Drag coefficient of single bubbles rising in biotechnologically relevant fluids containing (in)organic compounds

G. Boomaars, R. Volger, C. Haringa

TU Delft Universiteit Leiden

Drag coefficient of single bubbles rising in biotechnologically relevant fluids containing (in)organic compounds

The effect of the sodium salts NaCl and Na2SO4, the protein albumin and egg-white protein on the drag coefficient of a single bubble in water

By

Greetje Boomaars

Student number Delft/Leiden: 5424933/s2876981

Daily supervisor: Ir. Rik volger

Supervisor: Dr. ir. Cees Haringa

2nd Examiner: Dr. Bijoy Bera

Project duration: September, 2023-November, 2023

Faculty: Faculty of Applied Sciences, Delft

Abstract

Understanding the dynamics of bubbles in broth is crucial for various biotechnological processes conducted in bubble columns, such as the manufacturing of cultured meat. In this study, the drag coefficient of individual bubbles ascending in sodium chloride, sodium sulphate, albumin, and egg-white protein solutions was determined. This was accomplished by extracting bubble characteristics, such as the equivalent diameter and terminal velocity, from images captured by a camera system, utilizing bubble detection by a software suite. The obtained terminal velocities and computed drag coefficients were then compared to existing predictive models developed by Clift, Fan and Tsuchiya, Ishii and Zuber, and Peebles and Garber. This comparative analysis was conducted to assess the accuracy of these models in predicting bubble behavior in contaminated water. The results indicated that the drag coefficient of single bubbles rising in salt and protein solutions is higher compared to when ascending in demineralized water. The drag coefficient of single bubbles rising in protein solutions predicted by the drag model of Ishii and Zuber aligned well with the experimentally derived drag coefficients. However, both drag models tended to underpredict the drag coefficient of bubbles ascending in protein solutions. In the case of salt solutions, the drag coefficient predictions by Peebles and Garber approached the experimentally derived drag coefficients more closely although both models tended to overpredict the drag coefficient of bubbles ascending in salt solutions. Additional data acquisition of bubbles within the same size distribution rising in the examined salt and protein solutions is needed to validate and further refine these observations.

Contents

Nomenclature

Notation

Re	Reynolds number
Mo	Morton number
Eo	Eotvos number
We	Weber number
F_D	drag force
F_b	buoyancy force
F_{VM}	virtual force
F_H	Basset force
C_D	drag coefficient
V_g	equivalent bubble volume
d_{eq}	equivalent diameter of bubble
g	gravity acceleration
v_T	terminal velocity
L	distance between bubbles in subsequent frames
x_i, x_{i-1} y_i, y_{i-1}	coordinates of the bubble
Δt	time difference between subsequent frames
d_n	inner diameter of the capillary nozzle
$\Delta\rho$	density difference between gas and liquid

Greek letters

ρ	fluid's density
μ	fluid's viscosity
σ	surface tension
μ_{ref}	0.0009kg/(m·s)

Subscripts

g	gas
l	liquid

1

Introduction

Biotechnology concentrates on using bioprocesses by living organisms like bacteria, fungi and algae, single cells or enzymes for production, transformation and degradation [1], [2]. Examples of biotechnological processes are the fermentation of syngas and the production of cultured meat. These bioprocesses are often held in multiphase bubble columns due to their efficient mixing, low energy intake, simple construction, low operation and maintenance cost, and good gas-liquid heat transfer [3]–[5]. Because gas-to-liquid mass transfer is often the limiting factor in the capacity of the bioreactor, bubble dynamics and flow regimes have a crucial impact on the scale-up, design and profitability of bioprocesses [6]–[8]. The behavior of bubbles is controlled by the drag force and can be described by characteristics such as the bubble's shape and size, the bubble rise velocity and its movement pattern. The bubble rise velocity is the pre-dominant quality and next to that, an indirect adjustable parameter due to its extreme sensitivity to the physical properties of the reactor medium which depends on the solutes in the water [7], [9]–[11]. Computational fluid dynamics (CFD) is implemented to simulate the motion of different phases through each other by using models based on conservation laws. In this way, the gas-liquid flow of air bubbles through water has been analyzed which is a crucial element for a successful operation in bubble columns on the industrial scale [5], [12]. However, surfactants are present in the broth of bioprocesses which influence physical properties like density, viscosity and surface tension of the fluid medium and the volumetric mass transfer coefficient [6]. Since it is not accurate to simply modify the CFD models of bubbles in water by only taking into account the alternative liquid physical properties, it is important to examine the effect of these solved compounds on the bubble flow behavior [13]. So in this paper, the effect of various salts and proteins on the drag coefficient of a single rising bubble is studied. Eventually, the outcomes will be compared to current models that describe flows by predicting the corresponding drag coefficient.

1.1 Bubble dynamics

Bubble behavior can be described by interphase forces that regulate the interaction between the dispersed gas phase and the continuous liquid phase when in laminar flow, involving particles proceeding cohesively at low pace [11], [14], [15].The bubble rise velocity is a result of the net force working on the bubble, according to Newton's second law of motion [16], [17]. To compose this net force, all forces between the relatively moving liquid and gas must be taken into account. The gravity force can be ignored due to the small weight of bubbles [18]. Forces that act up between the phases are drag, lift, turbulent dispersion, virtual mass, Basset, buoyancy, Saffman force and pressure gradient [19]. Drag force is the force opposed to the bubble motion due to the resistance experienced by a bubble moving through a liquid [17], [20]. Moreover, the lift force is the perpendicular component of the drag force that works in transverse direction from the way the bubble is moving. It considers the result of the shearing motion on the travelling bubbles. In addition to drag and lift force, the turbulent dispersion force includes the turbulent flows in the liquid acting on the gas volume fragment because the velocity of the fluid varies consistently and arbitrarily. It

includes the impact turbulent swirls in the liquid phase have on the bubbles. Then, forces because of the increasing speed of the liquid when a bubble is dispersed, are the virtual mass force and the Basset force. The virtual mass force is the force acting on the accelerating fluid by the bubble [11]. On the contrary, the Basset force is the force on a bubble because of the delay of progression of the boundary layers with the acceleration of the bubble. It comprises the viscous phenomena [17]. Furthermore, the buoyance force is the force on the bubble that is dispersed in fluid and is proportional to the mass of the fluid replaced by the bubble [21]. Interphase forces due to existing velocity, pressure or temperature gradients in a flow, work on bubbles moving through these gradients. The Saffman force is a lift force working on bubbles with constant velocity travelling in areas with a velocity gradient. It arises from the consequences of inertia in viscous flow [17]. The pressure gradient force comes from a difference in pressure across a surface. These interface forces are influenced by the fluid properties which differ per solute.

In this project, single bubbles will be analyzed to prevent complexation due to bubble-bubble interactions. In this way the effect of the solutes on the interface forces can be examined. After releasing one bubble, it will accelerate until a steady-state speed is reached. From then the bubble will proceed with its terminal velocity. From that moment, the slip velocity, the difference between the average velocities of two different fluids flowing together in a pipe, is constant so the bubble moves uniformly. Now, the total drag force is mostly of influence, working downwards [11]. Its opponent is the buoyance force, acting in upward direction and resulting in equilibrium [4], [12], [16], [19], [22]. The forces acting on a single bubble rising in fluid are represented in Fig. 1. The total drag force consists of the drag, virtual mass and Basset force. The virtual mass force is responsible for the form drag because of the increase in speed and the Basset force withholds the viscous effects [14], [20]–[22]. Disregarding all forces except from the total drag and buoyance force also result in the minimization of computational costs [11]. These forces are a subject to fluid qualities and the bubble size and influence the progression of the ascending bubble [4].

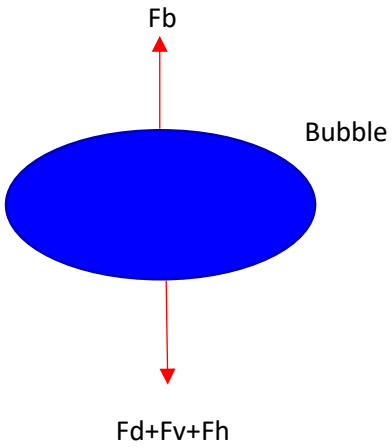

Figure 1 The interphase forces acting on a single rising bubble.

1.2 The effect of surfactants on bubble behavior

Compared to current studies available on the behavior of air bubbles, the medium of bioreactors often is not pure water but contains (in)organic compounds. For example, cells frequently die due to mechanical perturbations, substrate depletion, the buildup of byproduct, viral infections and most notably, hypoxia [25]. This cell death results in the excretion of compounds, mostly proteins. Next to that, cells need substrate for maintenance, growth and production. For example, cells of mammals use Bovine Serum Albumin (BSA) for functioning. This serum is a by-product of conventional meat

production and contains growth factors, hormones, amino acids and lipids [26]. Apart from proteins, fermentation broths such as the medium of the Fisher-Tropsch process often contain salts to control pH, as nutrients, as well as anabolic and metabolic regulators for the cells [6], [27].

Research of Prins and van 't Riet on foam forming led to insights about the influence of protein additives present in the water medium on bubble properties. Surfactants, surface active agents, will adsorb at the gas-liquid interface with their hydrophobic parts while their hydrophilic parts will extend in the broth. This accretion of molecules influences the bubble dynamics by changing its superficial flexibility, viscosity, velocity as well as its deformation [7]. The amount of assimilated fragments to the bubble will decide its surface tension. Interfacial tension gradients prevent the surface from moving, making bubbles more rigid and spherical. The narrower the diameter of the bubble, the more rigid its surface becomes due to matching the shear stress exerted on the surface by the liquid. This results in less internal circulation and a slower rate of exposure between gas and liquid thus a smaller mass transfer coefficient [28]. Proteins are able to stabilize interfaces between colliding bubbles, prohibiting them from coalescence which results in a decrease in bubble diameter and hereby the promotion of mass transfer [6], [29], [30]. Moreover, the bubble's motion becomes less oscillatory due to its reduced size. As said before, polar sites of the adsorbed compounds will be positioned towards the water medium. In this way adsorbed surfactants will form hydrogen bonds with the medium. This results in less shear between the gas and liquid inducing a higher superficial viscosity. The ratio of hydrophobic to hydrophilic zones in the dissolved molecules determine to what extent it interconnects with water so also to what extend it will lower the bubble's (terminal) rise velocity [9]. Studies on the addition of ethanol to the syngas fermentation broth provided understanding of the effect of added alcohols and electrolytes on bubble behavior. These outcomes can be used to predict the behavior of bubbles in salted solutions. The addition of alcohols and electrolytes prevented bubbles from colliding leading to a reduction in bubble size. This caused bubbles to rise slower. With this, the gas hold-up together with the mass transfer increased [6]. The viscosity of salt solutions matches that of water [31].

The rate of the changes caused by additions to the medium depends on the type of medium component, its concentration but also on time and height because this relates to the amount of adsorbed molecules to the bubble surface [9]. The optimal salt and protein concentration in the medium depend on the organism used, the type of bioreaction and the conditions the process is held under. The protein medium concentration for the syngas fermentation usually lies in the range between 0.06-1.3g/L [6]. The albumin medium concentration for the production of cultured meat is around 0.8g/L [31]. However, J. Stout et al. came to the conclusion that a concentration of 3.2g albumin per liter medium provided the most favorable balance between cell growth and media cost [32]. Minerals present in the medium for the production of cultured meat are of very small magnitude, ranging from 0.000014g/L up to 0.5g/L [31]. So, to obtain a complete set of data, the effect of salt concentrations ranging from 0.075 to 0.300mol/L and of protein concentrations ranging from 0.50 to 2.0g/L will be examined in this experiment. Within this concentration range, four different concentrations will be investigated to identify potential plateaus in the observable trends.

1.3 Experimental approach

This study aims to investigate the impact of sodium chloride (NaCl), sodium sulphate (Na2SO4), protein from bovine serum albumin and from egg-white within an aqueous medium on the drag coefficient of individual ascending air bubbles. The drag coefficient is the parameter of interest because it is independent of the scale of the system. This way, the experimental results obtained in this project could be of use at larger scales more close to the industrial bubble column. To achieve this objective, the trajectory of a single bubble moving through the fluid will be documented by

capturing images from a single vantage point. The characteristics concerning shape and motion will be ascertained using image-processing software. The processing of the acquired data should result values for the bubble equivalent diameter and terminal velocity. In conjunction with the measured surface tension and viscosity parameters, these values facilitate the computation of drag coefficients. These coefficients, the computed terminal velocities and the calculated equivalent bubble diameters will be compared to their predictions derived from the equations outlined in the theoretical background In section 2. This comparative analysis serves to assess the accuracy of different theoretical models, leading to potential enhancements in the predictive capability of these models.

2

Theoretical background

2.1 Drag coefficient of a single rising bubble

The drag force is the predominant force concerning the bubble flow [7], [33]. Classical equations assuming bubbles are spherically shaped, state that the drag coefficient is a function of the dimensionless Reynolds number (Re). The Reynolds number represents the relationship between the forces related to a fluid's inertia and those linked to its viscosity when it experiences internal motion caused by varying fluid speeds [34]. Reynold's ratio is given in Eq. (1) below.

$$Re = \frac{inertia\ forces}{vicous\ forces} = \frac{vd_{eq}\rho}{\mu} \quad (1)$$

In this expression, v is the fluid's velocity, ρ its density and μ its viscosity. d_{eq} is the equivalent bubble diameter. For small objects, viscous forces are dominant and the flow is laminar which means that it does not increases its speed until it is unstable. The object than is also more rigid. For laminar flow, $Re \ll 1$ will hold. When $Re \gg 1$, the flow is turbulent and inertia forces are controlling [35]. An example of these prediction methods which hold only for low Re is the Stokes drag law. However, to develop CFD simulations, the classical drag coefficient is frequently adjusted to represent more compound flows [16]. For instance, Dhole et al., Feng and Michaelides and Kishore et al. computed drag models for round rising bubbles with mean Reynolds number. When the value of Re enlarges, rising bubbles will change forms. Then, the Navier-Stokes equation cannot provide adequate solutions. Improved drag models using Morton's (Mo), Eotvos' (Eo) and Weber's (We) number apart from Reynolds number do [7]. These models assume the alternating shapes of bubbles to be ellipsoidal, oblate ellipsoid, spherical cap, or saucer shaped [9]. Models that are interesting to compare to the data obtained in this experiment are the Ishii an Zuber and the Peebles and Garber model (Table 1). The Ishii and Zuber model applies to both pure and contaminated systems while the Peebles and Garber model solely applies to contaminated systems [33]. Since the drag prediction models are derived under steady-state conditions, only steady-state data and their estimations can be compared to these existing representations [7].

Expression	Formula	Reference	Remarks
$C_D = max\left\{\frac{24}{Re}(1+0.1Re^{0.75}), min\left[\frac{8}{3}, \frac{2}{3}\sqrt{Eo}\right]\right\}$	(2)	Ishii an Zuber	Pure and contaminated system
$C_D = max\left\{max\left[\frac{24}{Re}, \frac{18.7}{Re^{0.68}}\right], min[0.0257EoWe^2, 0.82Eo^{0.25}We^{0.5}]\right\}$	(3)	Peebles and Garber	Contaminated system

Table 1 Drag models.

The behavior of a single bubble rising through an infinite motionless medium with a constant velocity can be described by the two-fluid Eulerian-Eulerian method which is based on the momentum equation with balanced buoyance and total drag force [8], [33], [36]:

$$V_g \rho_g g \frac{dv_T}{dt} = F_b - (F_D + F_{VM} + F_H) \quad (4)$$

where V_G is the equivalent volume of the bubble which is the volume of a sphere with the same diameter. ρ_g is the density of the gas, g is the gravity acceleration, v_T is the terminal velocity of the bubble, F_b the buoyance force, F_D the drag force, F_{VM} the virtual mass force and F_H, the Basset force. The total drag force is a summation of drag, added mass and Basset force and a function of the drag coefficient, a dimensionless quantity which assesses a value to the resistance of a body in a fluid [36]. This coefficient is regulated by the bubble diameter, its terminal velocity and the fluid properties. When the diameter of the bubble is consistent, a constant drag coefficient can be applied to minimize the computational time [11]. If this is not the case, the drag coefficient can be calculated with Eq. (5) below.

$$C_D = \frac{F_D + F_{VM} + F_H}{(\frac{1}{2}\rho_l {v_T}^2)(\frac{\pi}{4}{d_{eq}}^2)} = \frac{4}{3} d_{eq} \frac{(\rho_l - \rho_g)g - \rho_g \frac{dv_T}{dt}}{\rho_l {v_T}^2} \quad (5)$$

In the equation above, ρ_l is the density of the liquid and d_{eq} is the volume-equivalent diameter, the diameter of a sphere that has the same volume as the bubble. Because the density of water and watery solutions is much larger than that of air, the drag coefficient equation can be reduced to the form given in Eq. (6) [16].

$$C_D = \frac{4 d_{eq} g}{3 {v_T}^2} \quad (6)$$

This calculated drag coefficient relating to a single rising bubble can be compared to the drag coefficient predictions computed with the correlations given in Table 1. .

2.2 Terminal velocity of a single rising bubble

Generally, the velocity pattern is divided in firstly an increase in speed, than a velocity drop and subsequently it should stay constant. Bubbles form at the tip of the capillary and let go when the buoyance force is bigger than the surface tension. When released, the initial velocity is zero so the drag force is too, causing a rapid increase in the bubble's speed. During this acceleration the drag force enlarges with velocity slowing the bubble down until it equilibrates the buoyance force. That is when the bubble's maximum velocity is reached. This all happens in a short period of time. In distillated water, the maximum bubble velocity is the terminal velocity, in solutions it is not. Then the bubble's velocity tends to become smaller with height and time due to the increasing adsorption of surfactant. This also is influenced by the kind of solute and its concentration.

The terminal velocity of a single rising bubble can be predicted using existing equations, as represented in Table 2. Clift et al. set up Eq. (7) to estimate a bubble's terminal velocity rising in water containing surfactants [37]. These additives in the water lead to a surface tension gradient, the Marangoni shearing stress, at the gas-liquid surface because of a non-uniform organization. This strain points in the other direction than the buoyancy force. A bigger bubble diameter results in a smaller superficial tension gradient so less of this Marangoni strain. The equation thus is a good estimation for large bubble terminal velocities. In the equation, σ is the surface tension of the medium and μ_{ref} is the 0.0009kg/(m·s). Moreover, the equation of Fan and Tsuchiya regards all bubble sizes rising in pure and contaminated systems. These predictions of a single bubble's rise velocity in watery solutions is compared to the actual terminal velocity calculated with Eq. (10) on the basis of the obtained data. For dispersed air in demineralized water, a bubble motion in both x- and y-direction should be observed. The coordinates of the bubble center, the perimeter and its area were established by the evaluation of the frames. The local velocities were calculated by firstly determining the distance between bubbles in adjacent frames using Eq. (9) and dividing the obtained

length by the time interval between the frames in Eq. (11). The obtained terminal rise velocity of a single bubble is not a constant but oscillates. Therefore its magnitude is computed in two ways, locally and averaged.

$$L = \sqrt{(x_i - x_{i-1})^2 + (y_i - y_{i-1})^2} \quad (9)$$

$$v_T = \frac{L}{\Delta t} \quad (10)$$

In these equations x_i, x_{i-1}, y_i and y_{i-1} are the coordinates of the bubble and Δt is the time difference between successive photos.

Expression	Formula	Reference	Remarks
$v_T^{Clift} = \frac{\mu_L}{\rho_{Ld_{eq}}} Mo^{-0.149}(J - 0.857)$ $J = \begin{cases} 0.94H^{0.747}, 2 < H \leq 59.3 \\ 3.42H^{0.441}, H > 59.3 \end{cases}; H = \frac{4}{3} Eo \cdot Mo^{-0.149} (\frac{\mu_l}{\mu_{ref}})^{-0.14}$	(7)	Clift	Bubble in contaminated system
$v_T^{FT} = (v_{T1}^{-n} + v_{T2}^{-n})^{-\frac{1}{n}}$ $v_{T1} = \frac{\rho_l}{K_b \mu_l} g {d_b}^2$ $v_{T2} = \sqrt{\frac{2q\sigma}{d_{eq}(\rho_l + \rho_b)} + \frac{(\rho_l - \rho_b) g d_{eq}}{2\rho}}$ $K_b = \max(12, K_{bo} Mo^{-0.038})$	(8)	Fan and Tsuchiya	Bubble in pure or contaminated system In pure system, $K_{bo} = 14.7$ and $n = 1.6$ In contaminated system, $K_{bo} = 10.2$ and $n = 0.8$ In compressible liquid, $q = 1.4$; otherwise, $q = 1.2$

Table 2 Terminal velocity equations.

2.3 Bubble diameter

The bubble diameter depends on the inner diameter of the capillary used. When the flow conditions are constant, the equivalent bubble diameter can be estimated by balancing the buoyance force and the surface tension force using Tate's Law which states that the mass of a bubble formed at a capillary tip is proportional to the radius of this nozzle [9], [38], [39]. In this way the bubble diameter can be firstly predicted using Eq. (11) below.

$$d_t = [d_n \sigma / (\Delta \rho g)]^{\frac{1}{3}} \quad (11)$$

In equation (11), d_n is the inner diameter of the capillary tip, σ is the surface tension of the medium-gas interface, $\Delta\rho$ is the density difference and g is the gravitation constant. The experimental diameter computed with the experimental outcomes of the software is compared with the diameter predicted by equation (11) to check the accuracy of the predicting skills of the equation.

2.4 Shape and motion of a single rising bubble

Studies such as Yan et al.'s on the behavior of air bubbles rising in water make a decent prediction for the bubble motion in the column used in this experiment. They show that small bubbles, with an equivalent diameter smaller than 1.4mm, follow a straight path and maintain an almost spherical shape. With increasing bubble diameter, the bubble's trajectory changes from straight to zigzag or spiral, while their form shifts from spherical to ellipsoidal or quasi-ellipsoidal until it leads to an

irregular shape. The progression of the bubble shapes in relation to Re is represented in Clift's diagram given below as Fig. 2.This zigzagging motion of rising bubbles arises due to vortex shedding and wake interactions [40]. It suggests the potential for periodic (terminal) velocity oscillations, which also results in an unsteady total drag coefficient [36]. Also, the bubble's orientation alternates when oscillating. The amplitude and frequency of the fluctuating bubble motion depends on the bubble's proportions, configuration and the presence of surfactants.

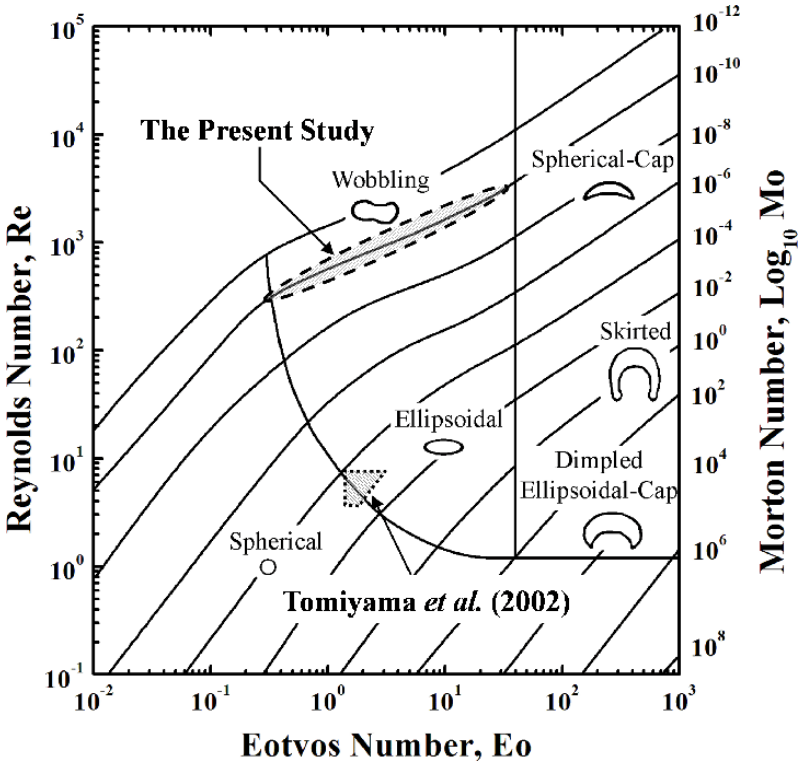

Figure 2 Clift's diagram [37].

3

Materials & Method

3.1 Bubble image acquisition

The experimental instruments for image acquisition comprised a video camera (Basler acA1920-150uc USB camera, up to 150 fps, at a resolution of 1920x1200 pixels) equipped with a 12mm C-mount Pentax lens, a data collecting system (Pylon 6 CoaXPress-12) and a software suite specialized in bubble property determination. The camera was positioned in front of a rectangular, transparent acrylic column (inner dimensions: 0.10x0.25x0.60m) in which the capillaries were adjusted. To ensure accurate imaging, the camera was carefully leveled, and its placement allowed for clear visualization of the nozzle tip, along with as much fluid above it as possible. The container was organized in front of a LED light panel (18W/25W, 1890lm/2735lm) from mlight, providing a uniform white background by illuminating. Three different capillaries (inner diameters (ID) of 0,254mm, 0,762mm and 1,76mm) were used to obtain different bubble sizes. Via flexible tubing, the capillaries were connected to a syringe pump (Qis), facilitating the controlled generation of bubbles for analysis. The experimental setup is represented in Fig. 3 below.

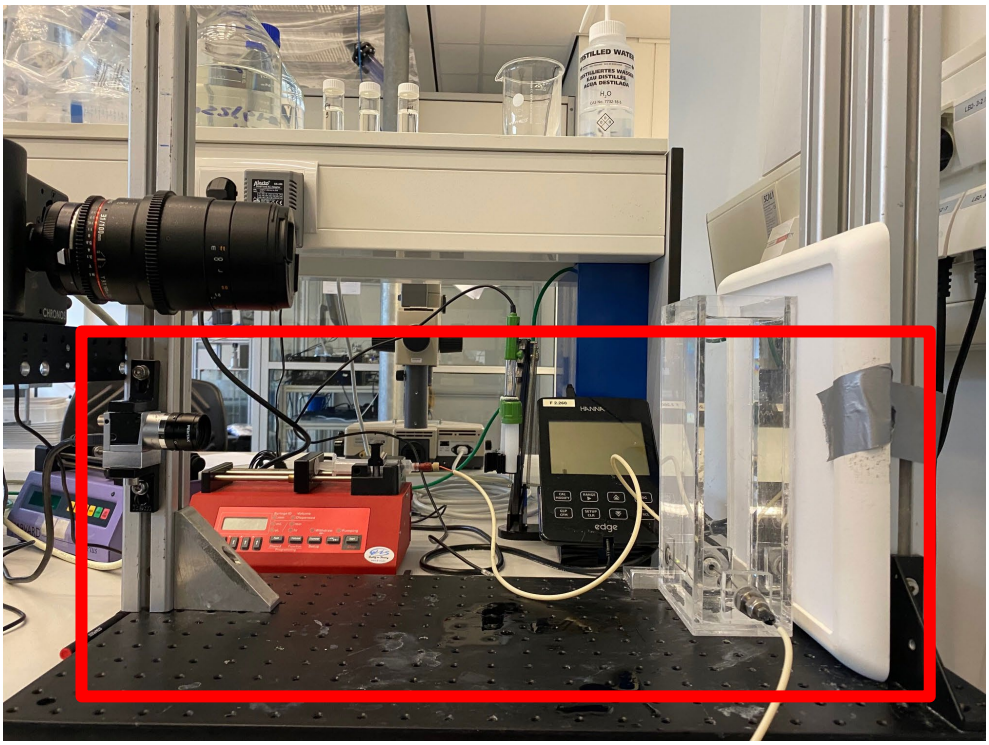

Figure 3 The experimental setup of the camera on the left (small one), the syringe pump (in red), the column and the light panel.

To capture high-resolution bubble images, the exposure settings were carefully managed. The camera's lens was adjusted to an intermediate aperture of f/8. The gain was set off and the exposure

time was installed at 1.0s. Within the Pylon program, the acquisition frame was enabled, operating at a rate of 100 frames per second (fps), and one frame was recorded for each acquisition. Furthermore, to reduce data size per frame, images were cropped and converted to black and white by setting the pixel format to mono 8. The recording of bubble behavior was terminated after 10 seconds, resulting in approximately 1000 frames per dataset. To prevent the computer from writing, the recording buffer size was set at a 1000 frames. To prevent data overflow, the recording buffer size was configured at 1000 frames. The syringe diameter was measured at 14.42mm, and this value was input into the pump settings. Specific airflow rate settings were established per measurement, enabling precise generation of individual bubbles.

All data was collected after a brief operational period of the system, ensuring that any potential gas holdup within the capillary, which might have otherwise affected the uniformity of the bubble production, was not considered. Ensuring a minimum of five bubbles was included in each measurement. A linear reference scale was positioned along the outer right side of the column, facilitating the conversion of pixel to SI unit distances for all datasets across their respective frames. In order to enhance our comprehension of the impact of individual components and operational parameters within the experimental configuration on air bubble behavior, preliminary measurements were conducted on isolated air bubbles rising in demineralized water. This preparatory study aimed to ultimately devise an optimal setup for the experiment. Initially, data was acquired concerning individual air bubbles emanated from the three capillaries ascending within a full column of deionized water to assess its potential effect on the bubble size created. This investigation encompassed three different volumetric flow rates (0.100, 0.500, and 1.000ml/min) per capillary. With the data obtained from the software processing, it was then decided if capillaries with distinct inner diameters actually generate bubbles of different sizes by comparing the mean equivalent diameter of the bubbles formed under different combinations of capillary dimensions and volumetric flow rate. After investigating the impact of the inner capillary diameter on bubble equivalent diameter, a more detailed examination was conducted to assess the effects of the volumetric flow rate. This procedure was conducted for each capillary by adjusting the syringe pump settings with finer incremental changes and analyzing the results with the specialized software. On the basis of the results of the research on the influence of inner capillary diameter and volumetric flow rate on the size of individually generated air bubbles, three specific combinations of capillary and syringe pump setting that produced bubbles of varying sizes were selected for further investigation. With the configured experimental setup, the impact of various salts (NaCl, Na2SO4, NH4Cl, and (NH4)2SO4) on individual ascending bubbles of air in water was examined across concentrations of 0.075, 0.150, 0.225, and 0.300 mol/L. Additionally, the influence of albumin protein and amino acids derived from egg-white protein on bubble behavior was investigated over a concentration range spanning from 0.5 to 2.0 g/L, with 0.5 g/L increments. Measurements at various concentrations were conducted across all three capillaries. The volume of demineralized water was measured with beaker glasses and the surfactant quantities were measured with a weighing scale (KERN, d=0.1mg). The solutions were mixed with a stirring rod. After shooting data, 50ml of each solutions was pipetted out for subsequent surface tension and viscosity measurements.

3.2 Bubble image processing

For dataset processing with the specialized software, truncated data frames were used, excluding the linear reference, column boundaries, and stationary bubbles. This encompassed the water surface containing both bubble reflections and, if present, any superimposed foam layers. So, as a pre-processing step, batch cropping was applied to each dataset using ImageJ. The software's ability to accurately detect bubbles from a specific dataset throughout the entire column height with the settings installed, was evaluated by executing the tuning function on three bubbles picked from the

dataset, one just after its release from the nozzle tip, one situated in the middle of the column, and one located at the top. The accuracy of the settings for a dataset was determined based on the absence of noise and the clear depiction of the specific bubbles in the images obtained from all tuning parameters. If the software demonstrated the capability to capture bubbles consistently along the entire column height for a particular dataset, the dataset's unique pixel-to-SI unit conversion values, derived from an ImageJ measurement of the scale reference, were properly configured, allowing for the execution of the code and subsequent data analysis.

Firstly, to assess whether the three chosen bubble sizes achieve their terminal velocity within the column height, velocity profiles were generated using the software-derived data from the three selected capillary and volumetric flow rate combinations after processing the data frames. Variations in the velocity were analyzed along the column height and compared to the amplitude of oscillatory motion observed in rising single air bubbles in water, as investigated by Yan et al. Additionally, the velocity profiles for individual bubbles were employed. The terminal velocity was determined by calculating the average of local bubble velocities observed within the steady state interval. Moreover, for each dataset a total velocity and equivalent diameter profile was computed over the column height. From the usable equivalent diameter measurements of the detected bubbles and the steady-state interval in the total velocity profile, the mean equivalent bubble diameter and the terminal velocity with their corresponding SEM were calculated by averaging the local values. The obtained equivalent bubble diameter and its terminal velocity were compared to their predictions and used to compute the correlated drag coefficient which also was compared to its predictions.

3.3 Surface tension measurements

Apart from the main experimental setup, a Bubble Pressure Tensiometer (BPT) Mobile (calibrated with surface tension of demineralized water at room temperature: 72.5mN/m) and a capillary viscometer from SI analytics (Cannon Fenske viscometer for the determination of the kinematic viscosity according ISO 3105, ASTM D 446 and BS 188, Xylem Analytics Germany GmbH, type: 51310, capillary no.: 100, apparatus no.: 1086008) were utilized to measure the surface tension and viscosity of the surfactant solutions. The start and stop surface age in the BPT Mobile were set at 10 and 20000ms and the surface tension was measured in 30 steps.

4

Results&Discussion

4.1 Bubble property determination in air-water system for setup tuning

The comparative analysis between the experimentally derived equivalent diameters computed by the software and bubble size measurements with ImageJ of bubbles generated with the three selected combinations of capillary and volumetric flow rate in demineralized water, is represented in Fig. 4 below. With ImageJ, the cross sectional diameter of the bubbles just after their release from the capillary so when they exhibited ellipsoidal shapes is computed manually. The figure tends to provide a projection of the accuracy of the software in its measurements. The large vertical error bars corresponding to the ImageJ measurements represent the range of light colored pixels around the dark pixels used as the bubble frame. As depicted in the graph, the bubble equivalent diameters of the relatively smaller bubbles computed with the software fall within the measured cross sectional equivalent bubble diameters of approximately 3.00, 4.00 and 4.70mm. However, the figure suggests a slight tendence of the software to underpredict the equivalent diameter of intermediate-sized bubbles and to overpredict the equivalent diameter of the relatively bigger bubbles. The possible overpredicting of the equivalent diameter of bigger bubbles can be attributed to their more deformable character as observed in the frames.

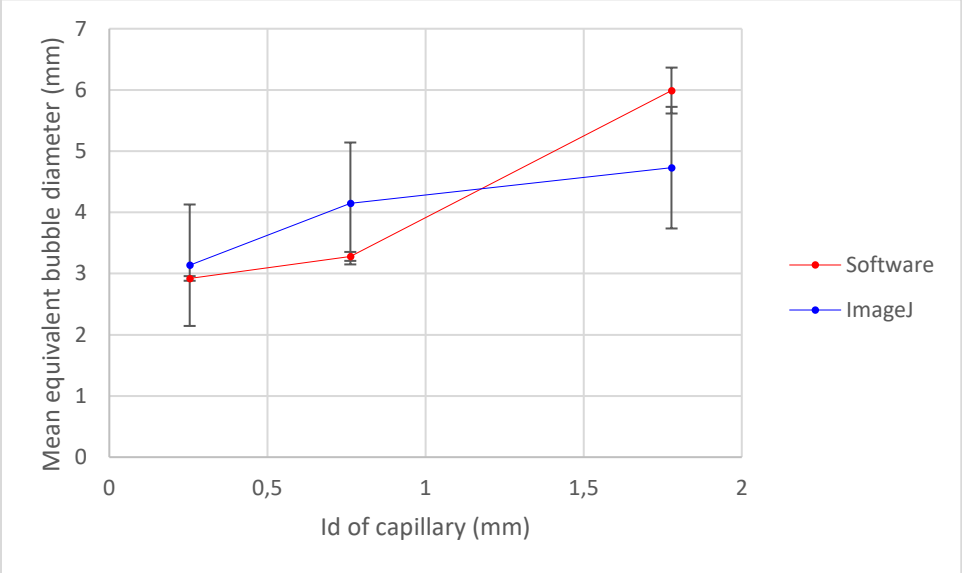

Figure 4 Comparison of mean equivalent diameter with its corresponding Standard Error of the Mean (SEM) of bubbles with distinct sizes generated with the three capillaries under a volumetric flow rate of 0.500ml/min computed by the software and the cross sectional equivalent bubble diameters measured with ImageJ. From a minimum of five bubbles per combination, the mean and SEM are calculated from the usable outcomes of bubble detections by the software ranging from 5 up to 57 per dataset. The error bars corresponding to the ImageJ measurements represent 6 pixels.

The experimentally derived mean equivalent bubble diameters are presented in Fig. 5 below. The figure provides a projection of the influence of the inner diameter of the capillary on the equivalent diameter of the bubble formed under varying volumetric flow rates (0.100, 0.500 and 1.000ml/min).

The relatively small vertical error bars signify the generation of bubbles with uniform equivalent diameters across the capillaries at consistent volumetric flow rate. The variation increases with enlarging equivalent bubble diameter, attributed to greater deformability which results in a fluctuating detectable diameter. Analyzing the morphology of the three graphs, reveals that under a volumetric flow rate of 0.500ml/min, bubbles with larger equivalent diameter were generated with capillaries having bigger inner diameter. This aligns with the expectations regarding Eq. (11), stating capillaries featuring a larger inner diameter are expected to generate bubbles with a greater equivalent diameter. However, under a volumetric flow rate of 0.100 and 1,000ml/min, the generated bubbles exhibited similar equivalent diameter. The largest bubbles, featuring an equivalent diameter of approximately 6.00mm, were generated from the capillary with inner diameter 1.778mm. The smallest bubbles, featuring an equivalent diameter of approximately 3.00mm, were formed at the capillary with inner diameter 0.254mm under a volumetric flow rate of 0.500ml/min. Furthermore, under volumetric flow rates of 0.100 and 1.000ml/min, the equivalent diameter of the bubbles formed, closely aligned. Moreover, with increasing the flow rate from 0.100 to 0.500ml/min, the equivalent diameter of bubbles generated with the capillary having the smallest inner diameter showed a slight decrease. Upon further increasing the volumetric flow rate, the equivalent diameter of the generated bubbles slightly increased. These fluctuating equivalent bubble diameters occurred within a 1.00mm range. Conversely, bubbles generated from the capillary with the largest inner diameter showed a noticeable initial increase and subsequent decrease in equivalent diameter with increasing volumetric flow rate, deviating with a maximum of 2.00mm. Higher flow rates generally reduce bubble size due to the limited bubble formation time caused by breakups of the emerging bubbles while lower flow rates extend the residence time of the bubble at the nozzle tip, facilitating additional growth before detachment. However, the slight divergent trends visible in the equivalent bubble diameter regarding the influence of the inner capillary diameter and volumetric flow rate, may be attributed to the outer diameter of the capillary. Apart from that, bubbles generated from the capillary with the intermediate-sized inner diameter exhibited a uniform equivalent diameter across the volumetric flow rates.

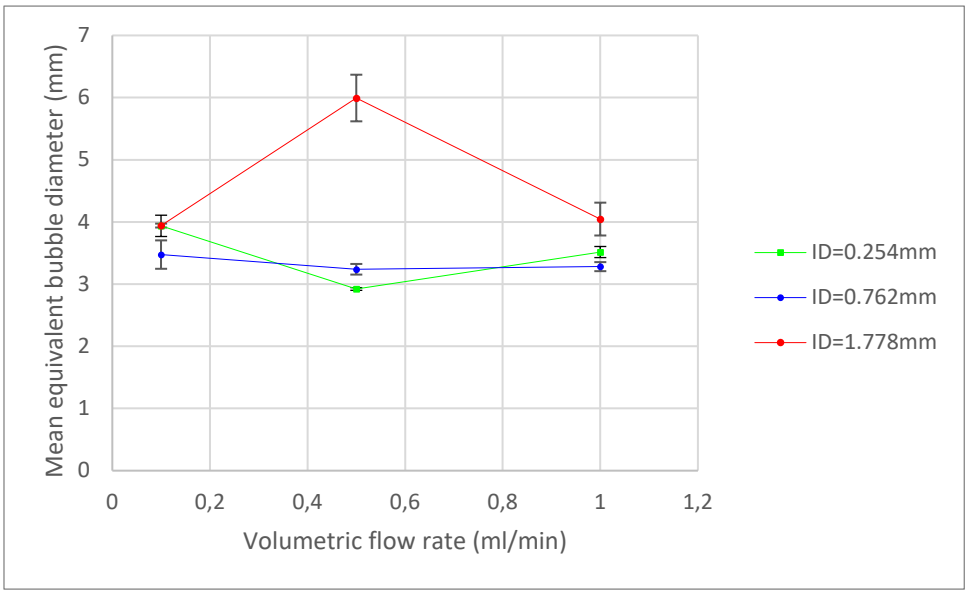

Figure 5 Mean equivalent bubble diameters with corresponding SEM at volumetric flow rates of 0.100, 0.500 and 1.000ml/min for capillaries with inner diameters of 0.254, 0.762 and 1.778mm. From a minimum of five bubbles per combination of capillary and volumetric flow rate, the mean and SEM are calculated from the usable outcomes of the bubble detections by the software ranging from 3 in the case of bubbles generated from the capillary with inner diameter 0.762mm under volumetric flow rate of 0.100ml/min up to 56 in the case of bubbles generated from the capillary with inner diameter 0.254mm under volumetric flow rate of 0.500ml/min per dataset.

The results of the study on the impact of volumetric flow rate on the equivalent diameter of the generated bubbles are represented in Fig. 6. The increasing magnitude of the vertical error bars with enlarging equivalent bubble diameter aligns with their more deformable character. Analyzing the morphology of the graphs reveals no distinct trend is discernible within and across the various capillary configurations. Consequently, for subsequent experiments, three specific combinations of capillary size and volumetric flow rate have been selected to yield bubbles with discernibly distinct sizes. In this subset, low volumetric flow rates have been considered to prevent the formation of bubble swarms while maintaining a rapid and consecutive generation of bubbles. The selected combinations are represented in Table 3.

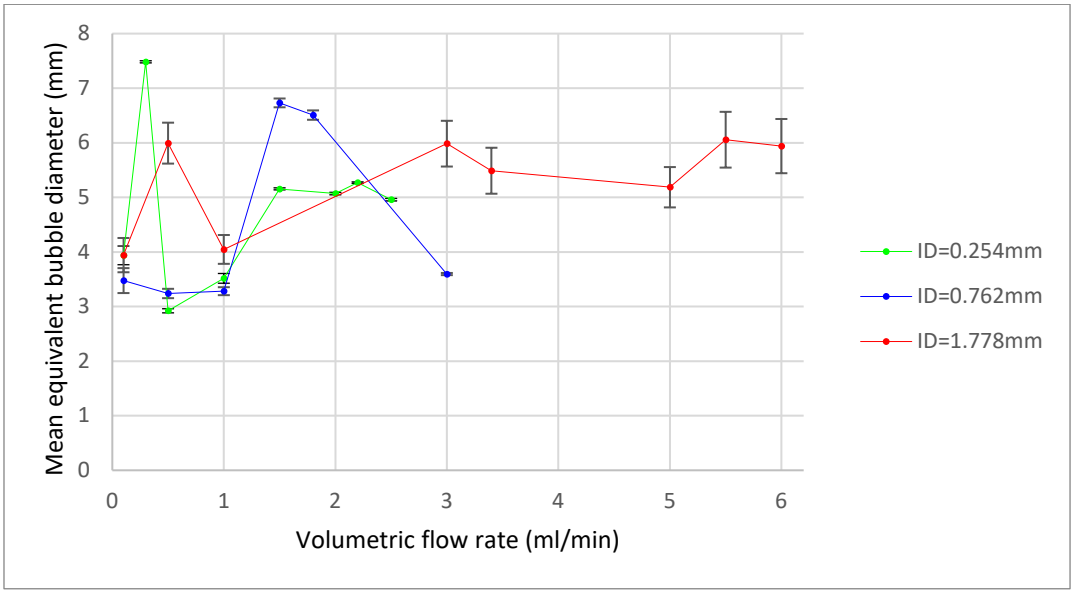

Figure 6 Mean equivalent bubble diameters with corresponding SEM at varying volumetric flow rates ranging from 0.100 to 6.000ml/min for capillaries having inner diameter 0.254, 0.762 and 1.778mm. Mean and SEM calculations are based on the obtained data for a range from 5 to 105 bubbles.

The velocity profiles of all detected bubbles generated with the three selected combinations of capillary and volumetric flow rate are represented in Fig. 7 below. The figure provides a projection of the progression of the detected bubbles. The outliers observed at approximately 0 and 20cm column height can be attributed to stationary bubbles present at the nozzle tip and the water surface. The noise around 4cm column height suggests a bubble resting at the column wall, confirmed by observations of the corresponding frames. Upon the exclusion of these outliers, Fig. 8 is derived.

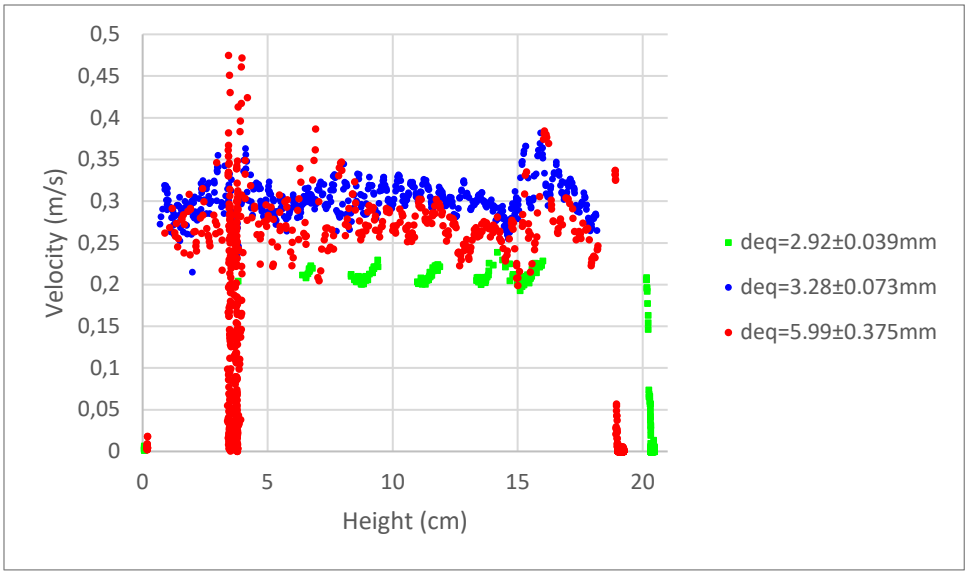

Figure 7 Velocity profiles of all detected bubbles, generated with the three selected combinations of capillary and volumetric flow rate, by the software within the column height. The calculated mean equivalent diameter of the bubbles is given in the legend with green representing combination 1, blue combination 2 and red combination 3. Mean and SEM calculations are based on the obtained data for a range from 11 to 56 bubbles.

The velocity profiles within the interval between 8 and 14cm column height extracted from Fig. 7 are represented in Fig. 8 below. The figure aims to examine whether the bubbles generated with the three selected combinations of capillary and volumetric flow rate reached steady-state within the column height. It can be seen that the velocity oscillations of the generated bubbles with distinct equivalent diameter align with the peak-to-peak amplitude ranging from 0.20 to 0.30m/s for the terminal velocity oscillations of equally sized bubbles established by Yan et al.'s study. Together with the stable oscillatory pattern, this suggests that all three bubble sizes attain a steady-state within the column height. The terminal velocity of the bubbles with the smallest equivalent diameter is the lowest, followed by the terminal velocity of the largest bubbles while the intermediate-sized bubbles exhibit the highest terminal velocity. Larger bubbles are expected to rise more slowly than smaller bubbles due to the prevailing influence of drag forces. This drag force increment emanates from the enlarged surface area and the transfer of a larger momentum from the bubble to the surrounding fluid which create more resistance to the bubble's motion. Additionally, flow separation induced by larger bubbles contributes to lower pressure drag, further accentuating the dominance of drag forces for larger bubbles. This phenomena can be seen for bubbles with the smallest and largest equivalent diameter although bubbles with the intermediate-sized equivalent diameter form an exception. The intermediate-sized bubbles ascending with the largest terminal velocity, suggest that the bubbles with an equivalent diameter around 3.28mm exhibit an optimal balance between buoyant and drag force, which allows them to rise more quickly compared to both smaller and larger bubbles. This optimum is likely related to the proportion between the bubble's shape and size which distinguishes the distribution of these two forces. Furthermore, the frequency of the observed velocity oscillations, which is consistent for all bubbles with distinct equivalent diameter, demonstrates an ascending pattern from the smallest to the intermediate and largest bubbles. This can be elucidated by the tendency of smaller bubbles to adopt a more spherical shape due to the elevated surface tension and reduced gravitational impact and inertia, making them less prone to deformations in their shape than larger bubbles and hereby resulting in less variation in local flow patterns around them.

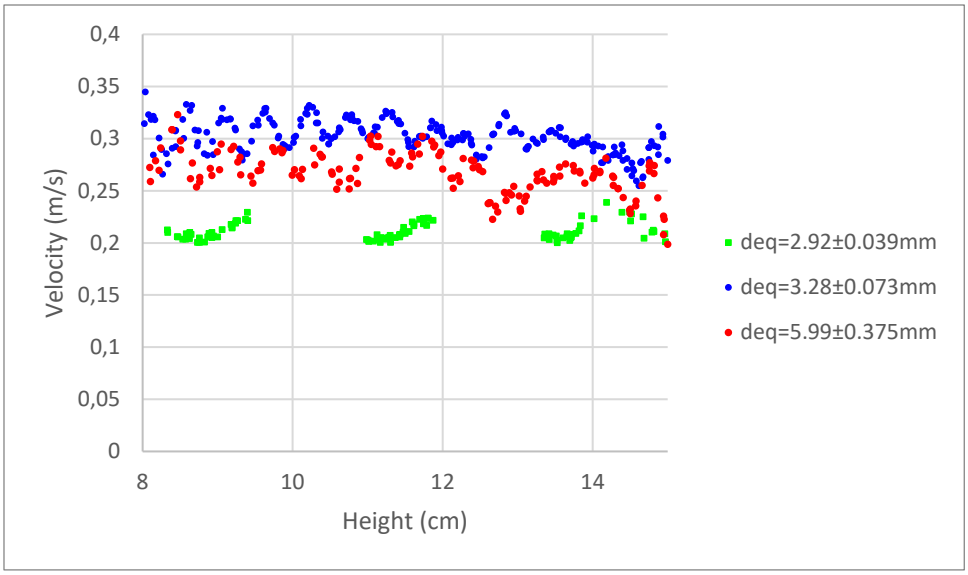

Figure 8 Velocity profiles of all detected bubbles, generated with the three selected combinations of capillary and volumetric flow rate, by the software within their steady-state interval in the column height. The calculated mean equivalent diameter of the bubbles is given in the legend with green representing combination 1, blue combination 2 and red combination 3.

The three selected combinations of capillary and volumetric flow resulting in the formation of bubbles with distinct equivalent diameter that attained a steady-state within the column height are given in Table 3 below. These selected combinations are used for further investigation on the effect of surfactants on bubble behavior.

Combination	Mean equivalent diameter and MES (mm)	n (amount of bubbles considered)	ID of capillary (mm)	Volumetric flow rate (ml/min)	Terminal velocity (m/s)	Re
1	2.92±0.038	56	0.254	0.500	0.2128±0.001136	617
2	3.28±0.073	11	0.762	1.000	0.3027±0.006270	990
3	5.99±0.375	57	1.778	0.500	0.2656±0.009145	1587

Table 2 The selected combinations of capillary and volumetric flow rate resulting in bubbles with three different equivalent diameters and terminal velocity, which values are given with corresponding SEM and the amount of detected bubbles that were taken into account for the calculation. Re is also given.

Upon a comparative analysis of the derived mean equivalent diameter of bubbles generated from the three capillaries with the experimental findings presented in the study conducted by Yan et al., it becomes evident that the capillaries with inner diameters of 0.254 and 1.778mm in this experiment yielded bubbles with somewhat bigger equivalent diameter, differing within a range of 1.70mm, and that the bubbles generated from the capillary with the intermediate-sized inner diameter exhibited an equal equivalent diameter. It is worth noting that their study used a volumetric flow rate range encompassing the one used in this study which may give different results regarding equivalent bubble diameter. Apart from a dissimilar volumetric flow rate, a difference in the outer diameter of the capillary and variations in the material of the capillary may result in bubbles with different equivalent diameter although having the same inner diameter. Thicker capillary walls have the potential to yield larger bubbles due to their capacity to accommodate increased flow rates and the provision of additional room for gas expansion during the bubble formation process. Additionally, capillary characteristics such as the wettability and surface roughness also impact the size of the bubbles formed from it. A smooth, hydrophobic material will for instance promote the formation of smaller bubbles.

The comparative analysis between the predicted equivalent diameters obtained with Eq. (11) and the experimentally derived equivalent diameter of bubbles generated with the three selected combinations of capillary and volumetric flow rate is represented in Fig. 9 below. The figure provides a projection of the accuracy of the equation in predicting the equivalent bubble diameter. It can be seen that only the predicted equivalent diameter of bubbles generated from the capillary with intermediate-sized inner diameter is equal to its experimentally derived equivalent diameter. The equation underpredicts the equivalent diameter of bubbles generated from the capillaries with the smallest and largest inner diameter, which values even fall outside of the 10% range from the predictions. This suggests a insensitivity to capillary-size dependent effects. The geometry of the capillary determined by the combination of inner and outer diameter, lead to different entrance effects. The capillary having inner diameter 0.254mm and a broader outer diameter could enable an increased curvature of the liquid-air interface which enhances surface tension effects. Together with the wider wetted area, the formation of somewhat bigger bubbles could be promoted.

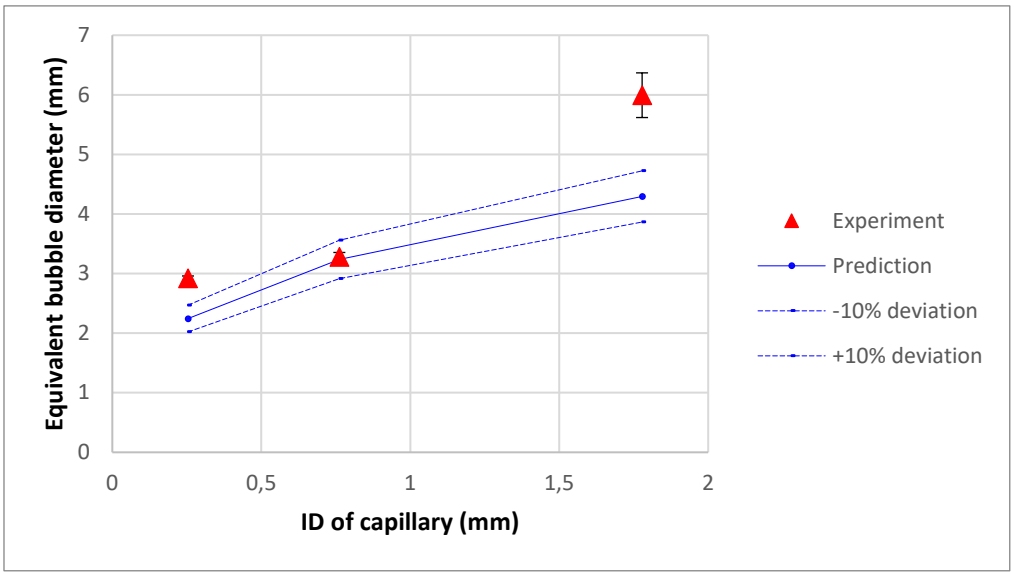

Figure 9 The predicted equivalent diameters with Eq. (11) and the experimentally derived equivalent diameter of bubbles generated with the three selected combinations of capillary and volumetric flow rate. Mean and SEM calculations are based on the obtained data for a range from 11 to 56 bubbles.

The comparative analysis between the terminal velocities predicted with Eq. (7) and (8) and the experimentally derived terminal velocities of bubbles generated with the three selected combinations of capillary and volumetric flow rate in demineralized water are represented in Fig. 10 below. The figures provide a projection of the accuracy of the equations in predicting the terminal velocity of bubbles rising in demineralized water. It becomes apparent that the terminal velocity prediction for bubbles with equivalent diameters around 2.92mm of Clift exhibits a stronger alignment with the experimentally derived terminal velocities. On the other hand, the terminal velocity for bubbles with an equivalent diameter around 3.28 and 5.99mm are better predicted by the equation of Fan and Tsuchiya. However, all predictions deviate between 0.50m/s from the experimentally derived values for the terminal velocity. Moreover, the terminal velocity predictions by Clift show an increasing trend with enlarging equivalent bubble diameter which agrees more with the trend in the experimentally derived terminal velocities. In contrast, the predictions of Fan and Tsuchiya demonstrate a decreasing trend in terminal velocity with increasing equivalent diameter. The observed trends in the predictions from the two equations imply that Clift overpredicts the effects of the drag force for smaller bubbles while tensing to underpredict these effects for larger bubbles. Fan and Tsuchiya assert a underestimation of the influence of drag force in the case of all

bubbles. Overall, Clift's terminal velocity predictions for these specific bubbles do exhibit a closer approach to the experimentally derived values, although with big deviations. The somewhat higher terminal velocity predictions derived from Fan and Tsuchiya's and Clift's equation in comparison to those in Yan et al.'s studies can be explained due to the use of slightly different values used for surface tension and density of water [36], [41].

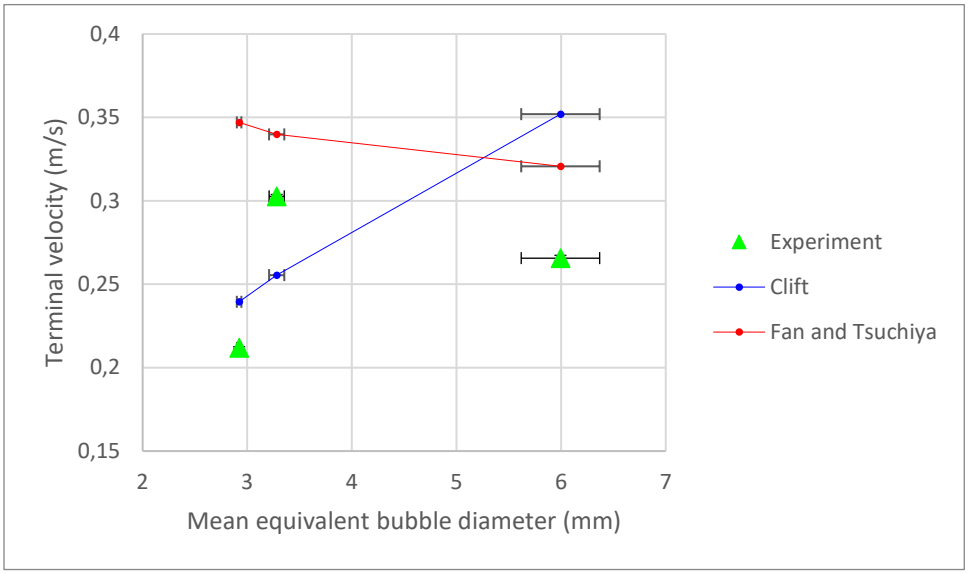

Figure 10 The predicted terminal velocities by Clift and Fan and Tsuchiya (Eq. (7) and (8)) and the experimentally derived terminal velocities of bubbles with distinct equivalent diameter generated with the three selected combinations of capillary and volumetric flow rate. Mean and SEM calculations are based on the obtained data for a range from 11 to 56 bubbles.

The experimentally derived drag coefficients, calculated from the obtained data of bubbles with distinct equivalent diameter generated with the three combinations of capillary and volumetric flow rate in demineralized water, are represented in Fig. 11 below. The figure provides a projection of the progression of the drag coefficients of the generated bubbles with different equivalent diameter when rising in demineralized water and their accordance with the study of Haberman and Morton [41]. The relative small vertical error bars, originating from the SEM associated with the experimentally derived equivalent diameter and terminal velocity of the generated bubbles, are negligible. This implies that the generated bubbles exhibit consistent drag coefficients, indicating that they possess a uniform shape which makes their behavior predictable. The larger vertical error bar relating to bubbles with Re of approximately 1600 suggest more substantial fluctuations in the equivalent bubble diameter. This aligns with the expectations and is in accordance with the observations within the frames. The morphology of the graph shows a decrease in equivalent diameter with increasing Re from approximately 600 to 1000, followed by an increase when further increasing Re to around 1600. This trend aligns with the relation between drag coefficient and Reynolds number for air bubbles rising with their terminal velocity in distilled water represented in the study by Haberman and Morton. However, the drag coefficient transition which is characterized by the de- and subsequent increase, is observed at lower Re of around 750 in the study of Haberman and Morton. Also, the minimum drag coefficient of 0.2 has a value twice as small as the calculated drag coefficient. This shift of the drag coefficient transition to higher Re, could be an indication of more irregular shaped bubbles experiencing higher drag forces.

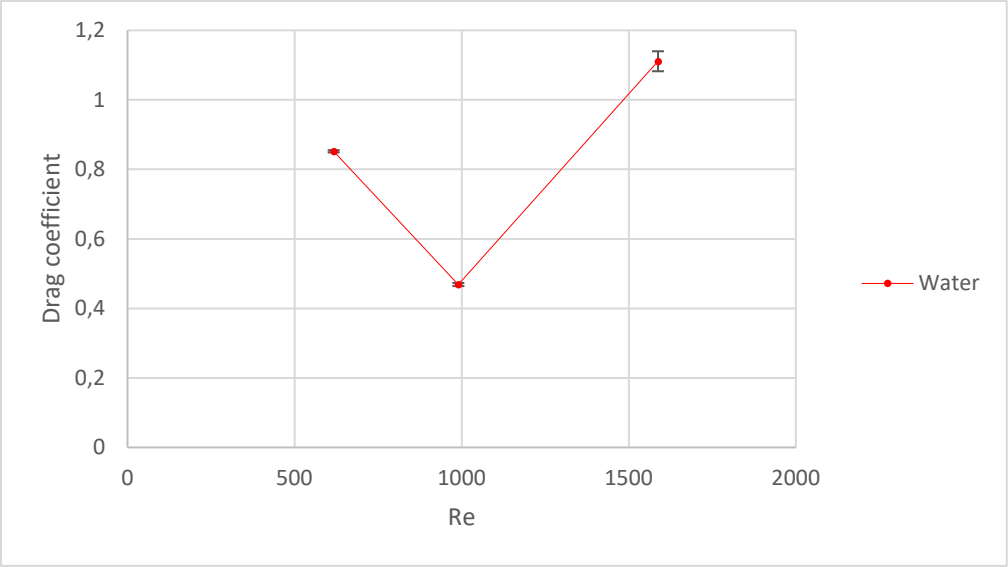

Figure 11 Experimentally derived drag coefficient of bubbles with distinct equivalent diameter generated with the three selected combinations of capillary and volumetric flow rate as a function of Re. Higher Re corresponds to bubbles with bigger equivalent diameter. Calculated drag coefficients are based on the obtained data for a range from 11 to 56 bubbles.

The comparative analysis between the drag coefficients predicted with Eq. (2), and the drag coefficients calculated with the experimentally derived data of the three distinct bubble sizes generated with the selected combinations of capillary and volumetric flow rate in demineralized water is represented in Fig. 12 below as a function of Re. The figure provides a projection of the accuracy of the model proposed by Ishii and Zuber in predicting the drag coefficient of bubbles with different equivalent diameter when rising in demineralized water. Firstly, the vertical error bars originating from the SEM associated with the calculated drag coefficients are negligible, stating bubbles with the same equivalent diameter and terminal velocity exhibit the same drag coefficient. This is an indication that these bubbles possess a consistent shape which makes their behavior more predictable. The slightly larger vertical error bar corresponding to the drag coefficient ratio predicted at Re of approximately 1600, corresponds to the more deformable shape of the larger bubbles. Analyzing the morphology of the drag coefficient ratios, reveals that the drag model underpredicts the drag coefficient of bubbles at Re below approximately 800 while overpredicting the drag coefficient at higher Re. The predictions at Re 600 and 1600 do show an approaching trend with regards to the experimentally derived drag coefficients. The decreasing trend in the drag coefficient ratio when increasing Re from approximately 600 to 1000 and the increasing trend upon further increasing Re, suggests the predictions converge with the horizontal line at 1 around Re 800 and possibly will do again at Re higher than 1600, signifying predictions congruent with the experimentally derived drag coefficient. The underprediction of the drag coefficient at low Re, corresponding to smaller bubbles, suggests the equation underestimates the drag force experienced by the bubbles with an equivalent diameter around 2.92mm when rising in demineralized water. the overprediction of the drag coefficient at higher Re, corresponding to bigger bubbles, indicates the overestimation of the drag force experienced by bubbles with equivalent diameters of approximately 3.28 and 5.99mm when rising in demineralized water. The trend in the drag coefficient ratios regarding the predictions of Ishii and Zuber show accordance with the trend observed in the study of Yan et al. However, as represented in the results of Yan et al., the equation of Ishii and Zuber underpredicted the drag coefficients up to a Re of approximately 1500, which is in contradiction with the observations in this experiment. This can be attributed to the different bubble sizes and shapes generated.

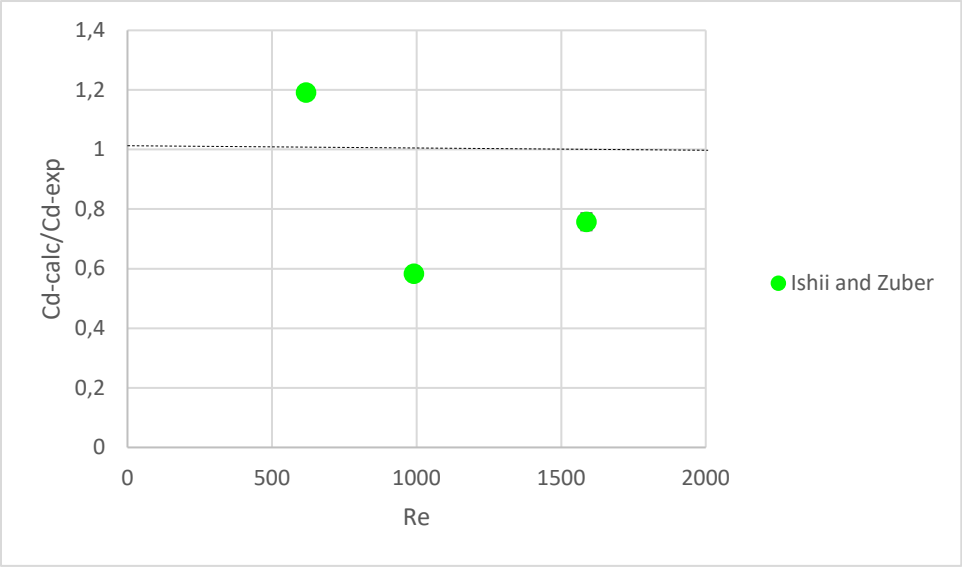

Figure 12 Ratio between predicted drag coefficients by Ishii and Zuber (Eq. (2) and the experimentally derived drag coefficients set against Re for the three bubbles with distinct equivalent diameter generated from the three selected combinations of capillary and volumetric flow rate. Higher Re corresponds to bubbles with bigger equivalent diameter. Calculated drag coefficients are based on the obtained data for a range from 11 to 56 bubbles.

4.2 Bubble property determination and drag coefficient calculation for salt solutions

The results of the surface tension measurements of the NaCl solution with a concentration of approximately 0.300mol/L, is represented in Fig. 13 below. The graph that stabilizes from 5000ms of surface age, indicates that the surface tension of NaCl solutions is slightly bigger than that of demineralized water, which is 72.5mN/m. This observation is consistent with expectations, as salt molecules interact with water molecules through ion-dipole interactions which weaken the cohesive forces between water molecules at the gas-liquid surface. However, a decreasing trend is observed for the Na2SO4 solution, although the surface tension did not yet stabilized within the measured surface age of 20000ms.

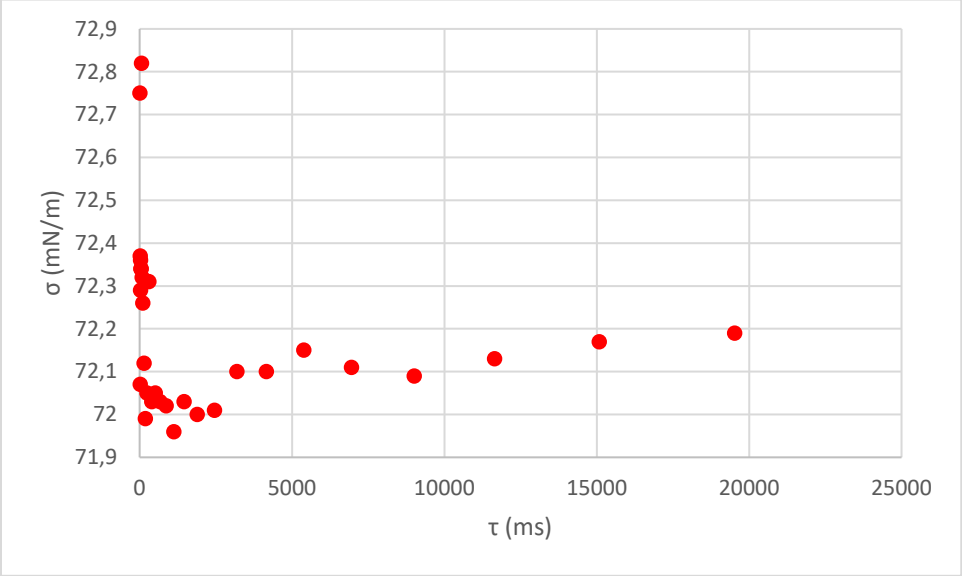

Figure 13 Measurement of the surface tension of a 0.300mol/L NaCl solution as a function of the surface age.

The mean equivalent diameters derived from the experimental results of bubbles generated with the three selected combinations of capillary and volumetric flow rate in NaCl and Na2SO4 solutions are

presented in Fig. 14 and 15 below. The figure provides a projection of the influence of salts on the equivalent diameter of bubbles rising through solutions with varying concentrations. The variations in salt concentrations stem from the fact that the measurements were held in alternative solutions. The relative large vertical error bars with a maximum of 1.00mm, illustrate the deformable character of bubbles rising in the salt solutions. The vertical error bars become larger with increasing equivalent bubble diameter. This can be attributed to the more deformable character of bigger bubbles. Analyzing the morphology of the graphs, reveals that the capillary with the largest inner diameter generated bubbles with slightly larger equivalent diameter in both NaCl and Na2SO4 solution while the two other capillaries generated equally sized, slightly smaller bubbles. From the order of the graphs it can be stated that both NaCl and Na2SO4 have a shrinking effect on the larger bubbles, with an initial equivalent diameter of approximately 5.99mm when rising demineralized water. From their increasing trend in equivalent diameter in NaCl solutions and the further decreasing trend in the equivalent diameter with increasing Na2SO4 concentration, it can be stated that the shrinking effect on larger bubbles is more pronounced in the Na2SO4 solution. The shrinking of bigger bubbles with increasing salt concentration while the surface tension decreases, suggests that the drag force becomes more dominant as the density of the fluid increases. The equivalent diameter of the two smaller bubbles generated with the two capillaries having the smallest inner diameter show only small fluctuations within 0.50mm over the concentration range in both salt solutions, indicating the further increase of the salt concentration from around 0.075 to 0.300mol/L is of little influence on the bubble size. Overall, bubbles rising in salt solutions exhibited a smaller size distribution in comparison to bubbles rising in demineralized water. The graphs suggest smaller bubbles with equivalent diameters between 3.00 and 5.50mm are favored in NaCl solutions and bubbles with equivalent diameters between 3.00 and 4.00mm are favored in Na2SO4 solutions.

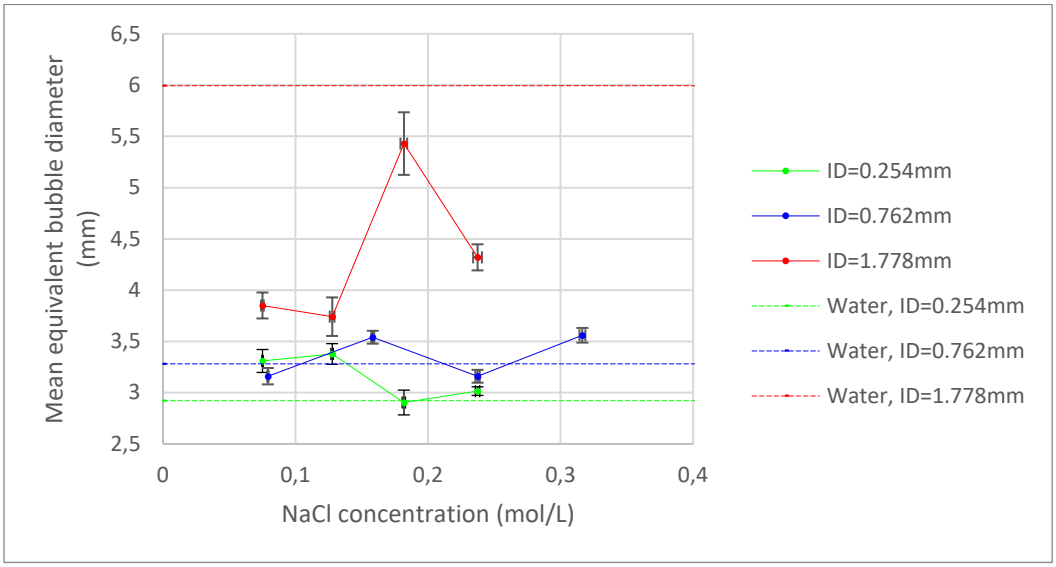

Figure 14 Mean equivalent bubble diameters with corresponding SEM of bubbles generated with the three selected combinations of capillary and volumetric flow rate in NaCl solutions with increasing concentration. The inner diameter of the used capillary is given in the legend with green representing combination 1, blue combination 2 and red combination 3. The calculated mean and SEM are based on the obtained data for a range of 5 to 18 bubbles.

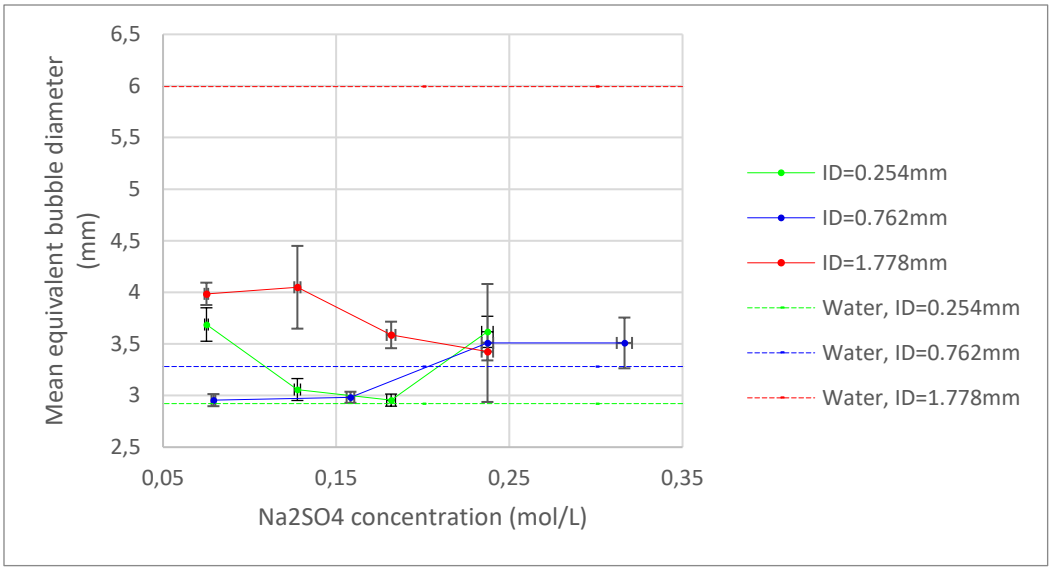

Figure 15 The mean equivalent bubble diameters with corresponding SEM of bubbles generated with the three selected combinations of capillary and volumetric flow rate in Na2SO4 solutions with increasing concentration. The inner diameter of the used capillary is given in the legend with green representing combination 1, blue combination 2 and red combination 3. The calculated mean and SEM are based on the obtained data for a range of 6 to 53 bubbles.

The comparative analysis between the terminal velocities predicted with Eq. (7) and (8) and the experimentally derived terminal velocity of bubbles generated with the three selected combinations of capillary and volumetric flow rate in NaCl and Na2SO4 solutions with increasing concentration are represented in Fig. 16 and 17 below. The figures provide a projection of the accuracy of the equations in predicting the terminal velocity of bubbles rising in salt solutions. The vertical error bars of the terminal velocity predictions by Clift and Fan and Tsuchiya have in the same magnitude as the vertical error bars of the experimentally derived terminal velocities. This suggests the possible oscillation of the terminal velocity within the same peak-to-peak amplitude. Analyzing the morphology of the graphs and datapoints, reveals that overall the equation of Clift underpredicts and the equating of Fan and Tsuchiya overpredicts the terminal velocities with equal deviations. This suggests the equation of Fan and Tsuchiya underestimates the drag force while the predications of Clift are likely to overestimate the effects of the increased drag forces experienced by the bubbles as a result of the decreased surface tension, leading to more deformable and sometimes bigger bubbles. However, the trend of decreasing terminal bubble velocity when rising in solutions with a higher salt concentration visible in the predictions of both equations, aligns with the experimental results. Furthermore, Fan and Tsuchiya's terminal velocity predictions show bigger differences between solutions with varying salt concentrations, which corresponds more closely with the experimental observations. Furthermore, better predictions are given by Fan and Tsuchiya for bubbles generated from the capillary with the smallest inner diameter while Clift more closely approaches the experimentally derived terminal velocities for bubbles generated from the capillary with the largest inner diameter.

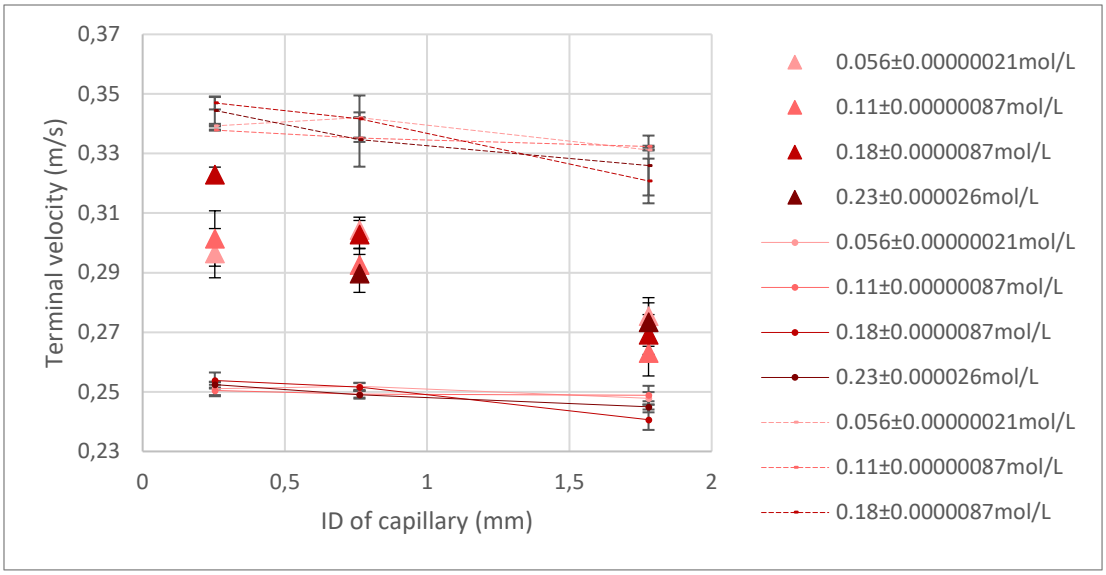

Figure 16 Comparison between the terminal velocity predicted with the equation of Fan and Tsuchiya (dotted graphs), with the equation of Clift (continuous graphs) and the experimentally derived terminal velocity (datapoints) of bubbles generated with the three selected combinations of capillary size and volumetric flow rate which rise in NaCl solutions with increasing concentration represented in the legenda. Higher salt concentrations are visualized with darker colors in this figure.

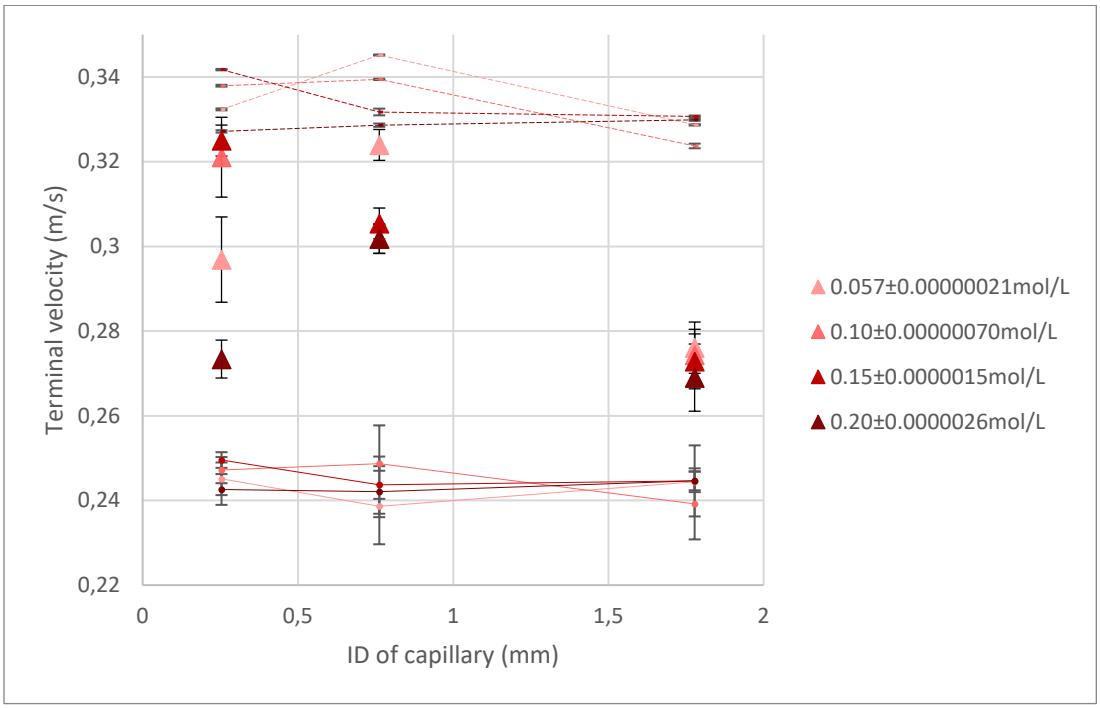

Figure 17 Comparison between the terminal velocity values predicted using the equation of Fan and Tsuchiya (dotted graphs), using the equation of Clift (continuous graphs) and experimental terminal velocity (datapoints) of the three selected combinations of capillary and volumetric flow rate resulting in three bubbles with distinct equivalent diameter rising in Na2SO4 solutions with increasing concentration (represented in legenda). Higher salt concentrations are visualized with darker colors in this figure.

The terminal velocity, calculated by averaging the local bubble velocities within the steady-state interval in the column, of bubbles generated with the three selected combinations of capillary and volumetric flow rate in NaCl and Na2SO4 solution are presented in Fig. 18 below. The figure provides a projection of the influence of salts on the terminal velocity of single rising bubbles. The divergent datapoint representing the terminal velocity of bubbles with an equivalent diameter of approximately 3.14mm in 0.300mol/L NaCl solution is attributed to the software's inability to

accurately capture the bubbles throughout the entire column height which possibly stems from the extreme fluctuating resolution of the bubble boarders. Consequently, this data point is disregarded in subsequent analyses. The relative small vertical error bars with a maximum of 0.02m/s, illustrates that bubbles rising in salt solutions with varying concentrations consistently reached a uniform terminal velocity oscillating within the amplitude of 0.10m/s observed for the terminal velocity of bubbles rising in demineralized water. This also suggests that the terminal velocity of bubbles rising in salt solutions oscillates less and is therefore more constant. This is in agreement with the observation in the frames. The quite constant magnitude of terminal velocity error bars over the salt concentration range suggests that increasing the salt concentration from 0.075mol/L on is non-influential to the oscillating terminal velocity. Moreover, the similar size of the terminal velocity error bars of bubbles in NaCl and Na2SO4 solutions suggest equal terminal velocity oscillations. Analyzing the morphology of the graphs reveals that the characteristics of the terminal velocities of bubbles rising in NaCl and Na2SO4 solutions are equal. Overall, the largest bubbles reach lower terminal velocity than the two smaller bubbles in both salt solutions. This is in alignment with the expectations. The increase in the terminal velocity of the biggest bubbles in both NaCl and Na2SO4 solution is in agreement with their reduced equivalent bubble diameter with respect to demineralized water. The terminal velocity of the smallest bubbles in demineralized water that have a slightly enlarged but almost equal equivalent diameter in the salt solutions, increased and aligns with the terminal velocity of equally sized bubbles generated from the capillary having the intermediate-sized inner diameter in water and the salt solutions. This discrepancy suggests a heightened influence of buoyancy forces. A plausible explanation is that slightly enlarged bubbles result in the displacement of a larger volume of water, contributing to the observed effect. The trend visible in the progression of the terminal velocity of the bubble with an equivalent diameter of approximately 3.17mm with increasing Na2SO4 concentration is in alignment with the trend in its mean equivalent diameter, represented in Fig. 15. The slightly decreasing trend of the terminal velocity of bubbles with increasing salt concentration with the exception of bubbles generated from the capillary having the smallest inner diameter, implies that the drag force becomes more dominant. This can be attributed to the increasing density of the fluid.

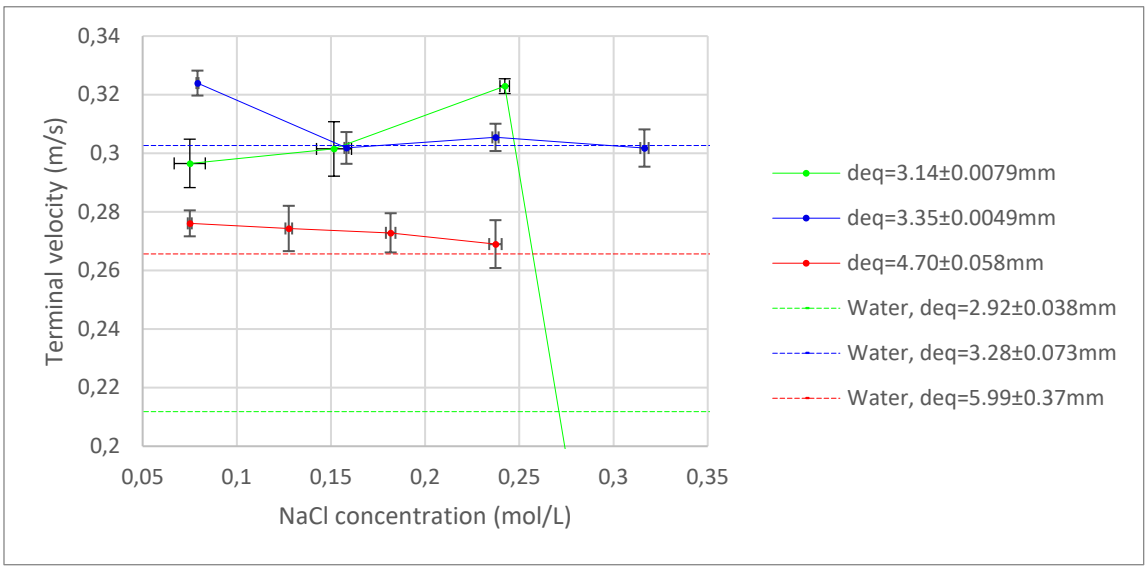

Figure 18 The terminal velocity with corresponding SEM of bubbles generated with the three selected combinations of capillary and volumetric flow rate in NaCl solutions with increasing concentration. The calculated mean equivalent diameter of the bubbles is given in the legend with green representing combination 1, blue combination 2 and red combination 3. The calculated mean and SEM are based on the obtained data for a range of 5 to 18 bubbles.

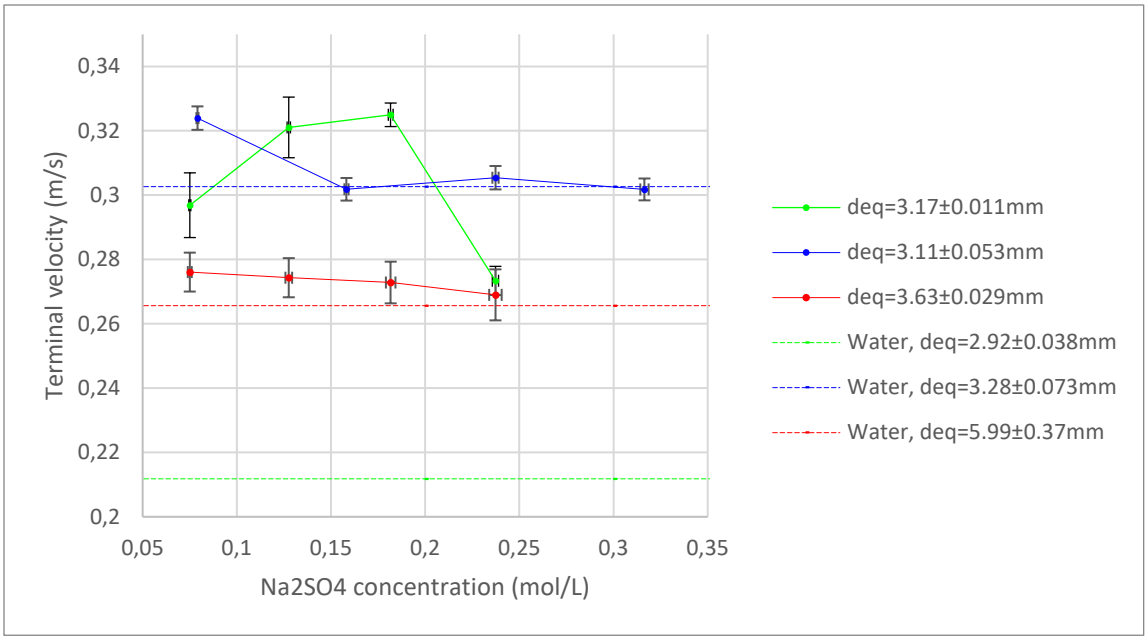

Figure 19 The terminal velocity with corresponding SEM of bubbles generated with the three selected combinations of capillary and volumetric flow rate in Na2SO4 solutions with increasing concentration. The calculated mean equivalent diameter of the bubbles is given in the legend with green representing combination 1, blue combination 2 and red combination 3. The calculated mean and SEM are based on the obtained data for a range of 6 to 53 bubbles.

The comparative analysis on the relationship between the drag coefficients predicted with Eq. (2) and (3) and the experimentally derived drag coefficients of bubbles generated with the three selected combinations of capillary and volumetric flow rate in NaCl and Na2SO4 solutions with increasing concentration is presented in Fig. 20 below. The figure provides a projection of the accuracy of the models in predicting the drag coefficient of bubbles rising in salt solution. Firstly, the vertical error bars originating from the SEM associated with the calculated drag coefficients are negligible, stating bubbles with approximately the same equivalent diameter rising in the salt solutions, exhibit the same drag coefficient. This is an indication that the formed bubbles with comparable equivalent diameter possess a consistent shape and are likely to have reached a uniform steady-state within the salt solutions which makes their behavior predictable. The horizontal error bars that become more prominent in the Na2SO4 solutions at high Re, are a result of the larger density deviations and reduction in surface tension in higher concentrated Na2SO4 solutions compared to NaCl solutions. This decreasing surface tension makes bubbles more prone to deformation leading to bigger indifferences in the equivalent bubble diameter and hereby also a more variating Re. Almost all drag coefficient ratios are situated below the horizontal line at 1, which represents the convergence of the prediction with the experimentally derived drag coefficient. This indicates an overall overprediction of the drag coefficient of bubbles rising in salt solutions by the two models. A reason for this could be that the models do not take the bubble deformability into account, which was visible for bubbles rising in salt solutions. Deformable bubbles are able to adapt to local flow, reducing flow separation and the experienced resistance when rising. However, it can be seen that the prediction of Peebles and Garber approach the experimentally derived drag coefficients of bubbles in NaCl solution with Re between 960 and 1060 and for bubbles in Na2SO4 solution with Re between 900 and 990. The model of Ishii and Zuber consistently overpredicts the drag coefficient of bubbles rising in salt solutions. However, the drag coefficient ratio of bubbles rising in NaCl solution at Re 1500 closely approaches the horizontal line at 1, which indicates the possible convergence of the drag model for Re higher than 1500. Furthermore, the increase of the drag coefficient ratio regarding the predictions of Peebles and Garber when decreasing Re from

around 1500 to 1000 regarding the NaCl solutions, indicate convergence at Re somewhat lower than 1000. This means the equation of Peebles and Garber predicts drag coefficients the most accurate for Re around 1000. On the contrary, the increasing trend in the drag coefficient ratios regards to the predictions of Ishii and Zuber when increasing Re from around 140 to 1500 with, suggest that the model of Ishii and Zuber gives better drag coefficient predictions at higher Re.

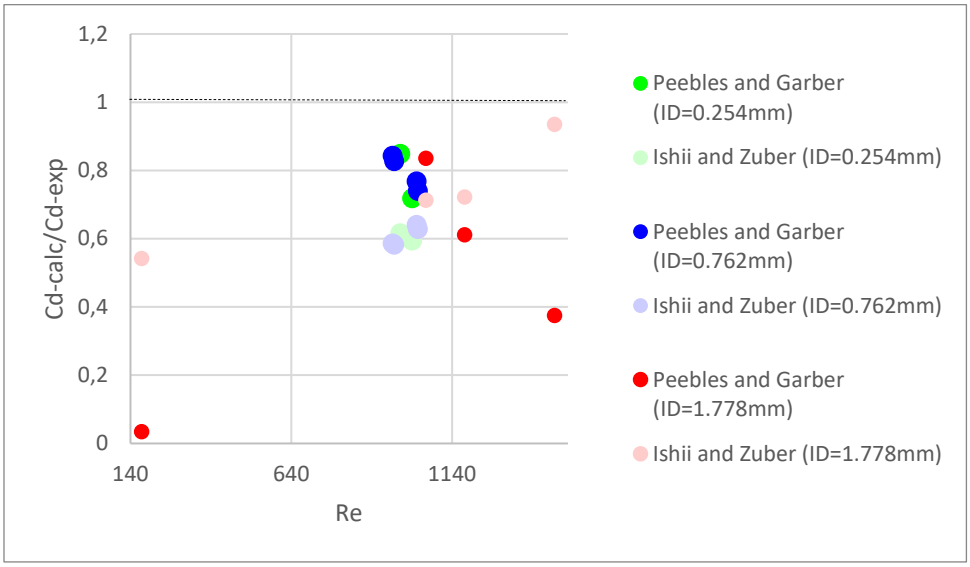

Figure 20 Ratio between the experimentally derived drag coefficients and drag coefficients predicted with the equations of Peebles and Garber and Ishii and Zuber (Eq. (2) and (3)) as a function of Re for bubbles generated with the three selected combinations of capillary and volumetric flow rate in NaCl solutions with increasing concentration. The calculations are based on the obtained data for a range of 6 to 53 bubbles.

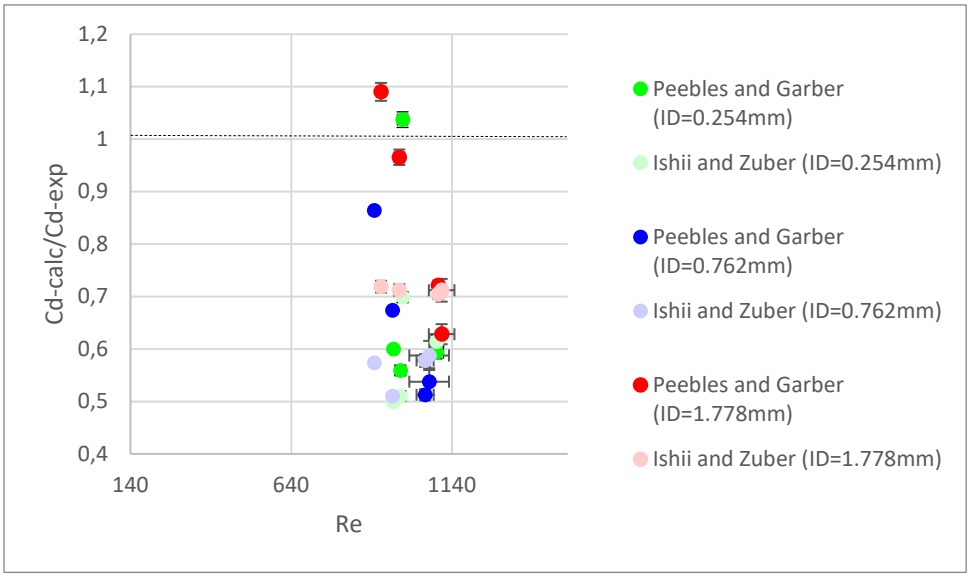

Figure 21 Ratio between the experimentally derived drag coefficient and drag coefficients predicted with the equations of Peebles and Garber and Ishii and Zuber (Eq. (2) and (3)) as a function of Re for bubbles generated with the three selected combinations of capillary and volumetric flow rate in Na2SO4 solutions with increasing concentration. The calculations are based on the obtained data for a range of 6 to 53 bubbles.

4.3 Bubble property determination and drag coefficient calculation for protein solutions

The surface tension of the albumin solution with a concentration of approximately 2.00g/L, is represented in Fig. 22 below. The graph that stabilizes from 5000ms of surface age, indicates that the

surface tension of albumin solutions surpasses that of demineralized water, which is 72.5mN/m. The same trend is observed for the egg-white solution.

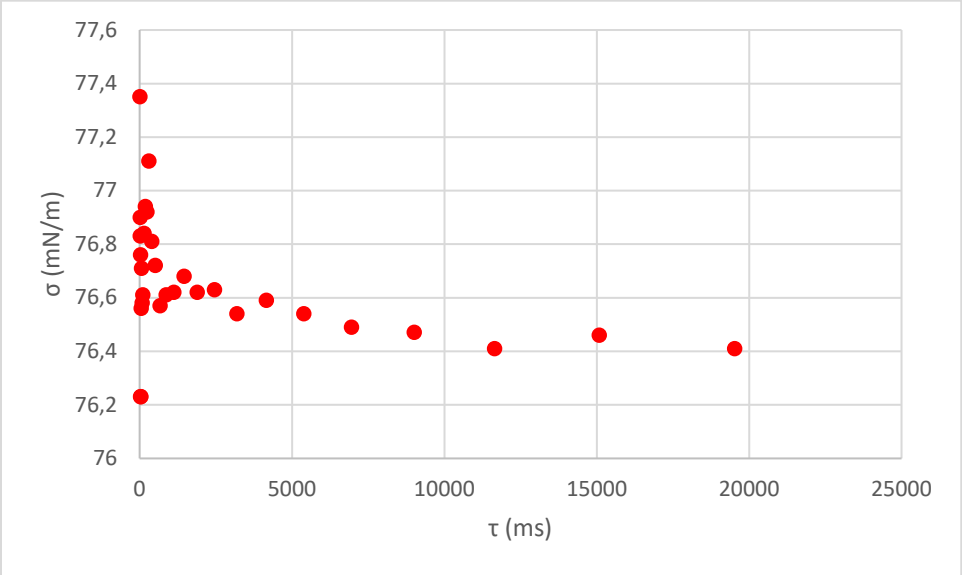

Figure 22 The surface tension of a 2.00g/L albumin solution as a function of the surface age.

The viscosity of a 2.00g/L albumin solution was measured slightly higher than that of demineralized water. This observation aligns with expectations. Large protein molecules contribute to heightened steric hindrance and the potential entanglement between the albumin molecules facilitated by hydrogen bonding, van der Waals forces and electrostatic interactions. Together with their higher molecular weight, it leads to an increase in hydrodynamic drag which imparts greater resistance to fluid flow. Additionally, the viscosity of the 2.00g/L egg-white protein solution was measured even slightly higher than that of the 2.00g/L albumin solution.

The mean equivalent diameter derived from the experimental results of bubbles generated with the three selected combinations of capillary and volumetric flow rate in albumin and egg-white protein solutions are presented in Fig. 23 and 24 below. The figure provides a projection of the influence of proteins on the equivalent diameter of bubbles rising through solutions with varying concentrations. The relative small vertical error bars with a maximum of 0.50mm, illustrate that all capillaries consistently generated bubbles with a uniform equivalent diameter in the protein solutions with varying concentration. Analyzing the morphology of the graphs, reveals that the equivalent bubble diameter enlarges consistently with increasing inner diameter of the capillary across the range of albumin concentrations while showing more overlap across the range of egg-white concentrations. This irregular trend in the equivalent diameter of bubbles in egg-white solutions extends itself in the bigger fluctuations between the equivalent diameter of bubbles generated with a specific capillary over the concentration range. The small fluctuations between the equivalent bubble diameters over the albumin concentration range, indicates the further increase of the protein concentration from around 0.50g/L to 3.00g/L is of little influence. From the order of the graphs it can be stated that both albumin and egg-white have a shrinking effect on larger bubbles, with an initial equivalent diameter of approximately 5.99mm when rising demineralized water. The two smaller bubbles generated with the two capillaries having the smallest inner diameter are almost unaffected by the presence of protein with the exception of increased equivalent diameter of bubbles generated from the capillary having the intermediate-sized inner diameter in a 0.80g/L egg-white solution and the bubbles generated from the capillary having the smallest inner diameter in a 1.50g/L egg-white solution. This indicates a possibility of the growing effects on smaller bubbles by the presence of egg-

white protein. Overall, bubbles rising in protein solutions exhibited a smaller size distribution in comparison to bubbles rising in demineralized water which indicates bubbles with equivalent diameters between approximately 2.5 and 5.0mm are favored. The stable trend of the equivalent bubble diameter with increasing albumin concentration and the quite stable equivalent diameter of bubbles generated with the two capillaries having the largest inner diameter when increasing egg-white concentration from 0.80g/L, suggests that the increasing density, surface tension and viscosity lead to an equal ratio between drag and Buoyancy forces.

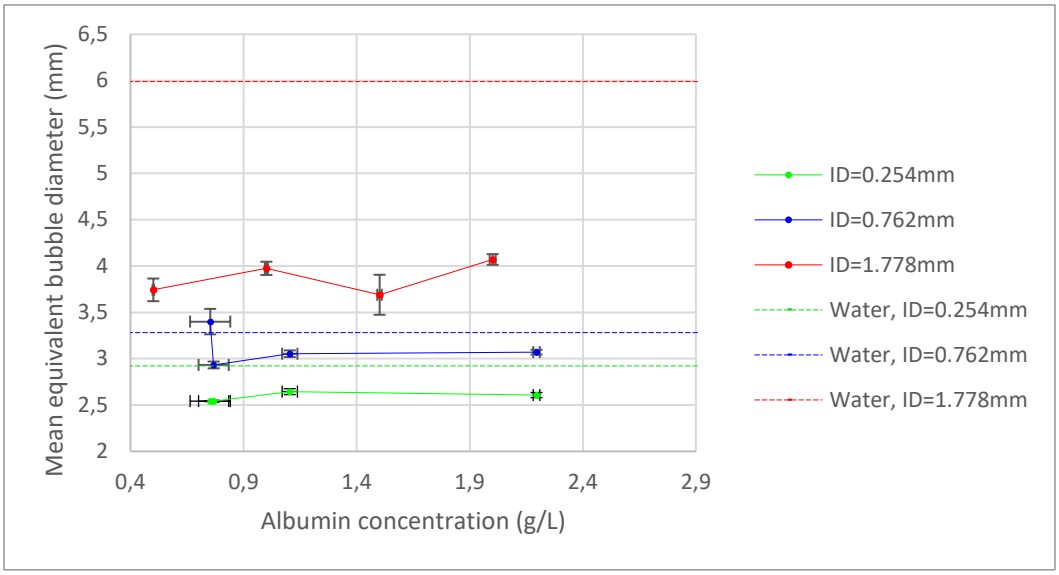

Figure 23 Mean equivalent bubble diameters with corresponding SEM of bubbles generated with the three selected combinations of capillary and volumetric flow rate in albumin solutions with increasing concentration. The calculated mean and SEM are based on the obtained data for a range of 5 to 69 bubbles.

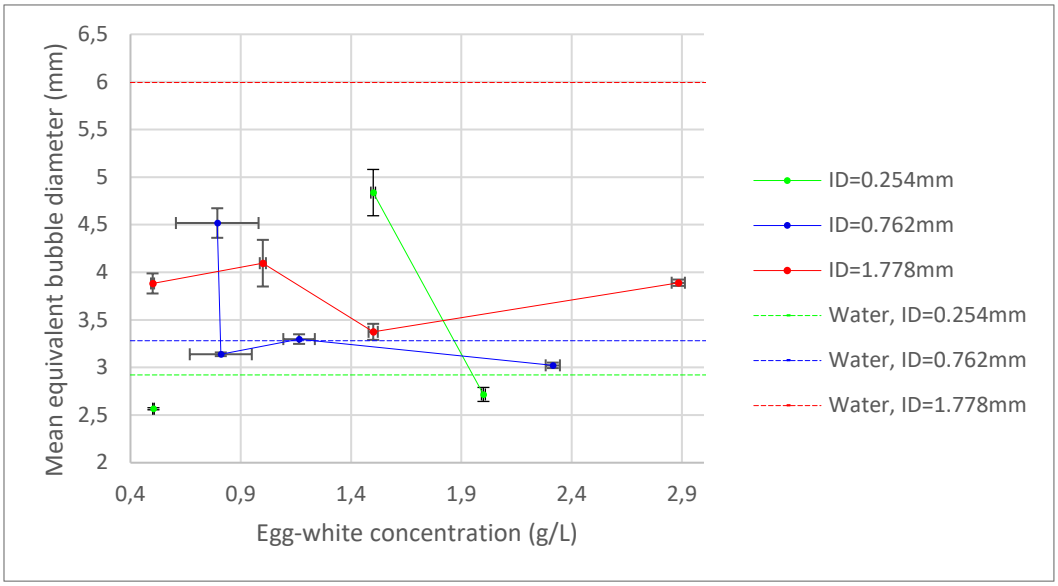

Figure 24 Mean equivalent bubble diameters with corresponding SEM for bubbles generated with the three selected combinations of capillary and volumetric flow rate in albumin solutions with increasing concentration. The calculated mean and SEM are based on the obtained data for a range of 3 to 90 bubbles.

The terminal velocities, calculated by averaging the local bubble velocities within the steady-state interval in the column, of bubbles generated with the three selected combinations of capillary and

volumetric flow rate in albumin and egg-white solutions with increasing concentration are presented in Fig. 25 and 26 below. The figure provides a projection of the influence of proteins on the terminal velocity of single rising bubbles. The magnitude of the vertical error bars with a maximum of , illustrates that bubbles rising in protein solutions with varying concentrations consistently reached a uniform terminal velocity oscillating within the amplitude of 0.10m/s observed for the terminal velocity of bubbles rising in demineralized water. The equally sized vertical terminal velocity error bars of the bubbles with an equivalent diameter of approximately 3.08 and 3.85mm when increasing albumin concentration, suggests that the oscillatory motion of these specific bubbles stays constant. The slightly decreasing magnitude of the vertical error bars corresponding to the terminal velocity of bubbles with an equivalent diameter of approximately 2.59mm when increasing the albumin concentration, indicates that the bubble motion becomes less oscillatory. The same is represented of the bubbles ascending in the egg-white protein solutions with increasing concentration. This also suggests bubbles rising in egg-white solutions oscillate less than in albumin solutions. This can be attributed to the higher viscosity of the egg-white solutions and is in agreement with the observations from the frames. Analyzing the morphology of the graphs reveals that overall, the two bubbles with the larger equivalent diameter reached a higher terminal velocity than the bubbles with the smallest equivalent diameter in both albumin and egg-white solutions, although the differences in equivalent bubble diameter are small. This can be attributed to their ability to overcome the increased viscosity. Overall, the bubbles in albumin as well as egg-white protein solutions reach terminal velocities of the same magnitude as bubbles with a similar equivalent diameter of approximately 2.92mm when rising in demineralized water. However, the few substantially lower terminal velocities present for bubbles rising in egg-white solutions suggest that egg-white reduces the speed of bubbles more. This can be attributed to their bigger increment in viscosity. Moreover, the trends visible in the progression of the bubble's terminal velocity with increasing protein concentration is in alignment with the trends in their mean equivalent diameter, represented in Fig. 23 and 24.

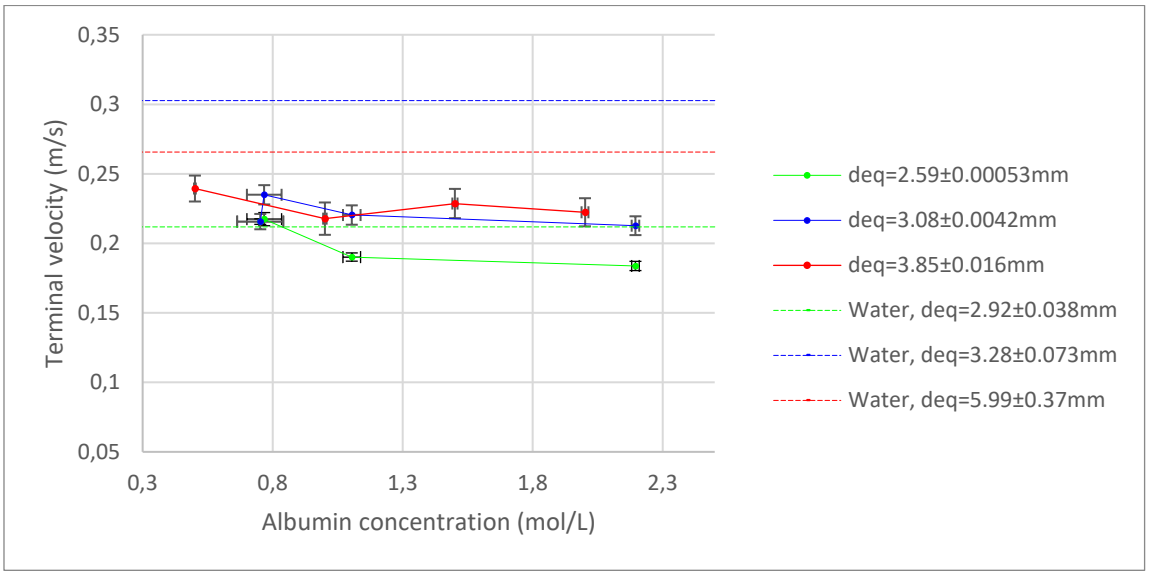

Figure 25 The terminal velocity with corresponding SEM for bubbles generated with the three selected combinations of capillary and volumetric flow rate in albumin solutions with increasing concentration. The calculated mean and SEM are based on the obtained data for a range of 5 to 69 bubbles.

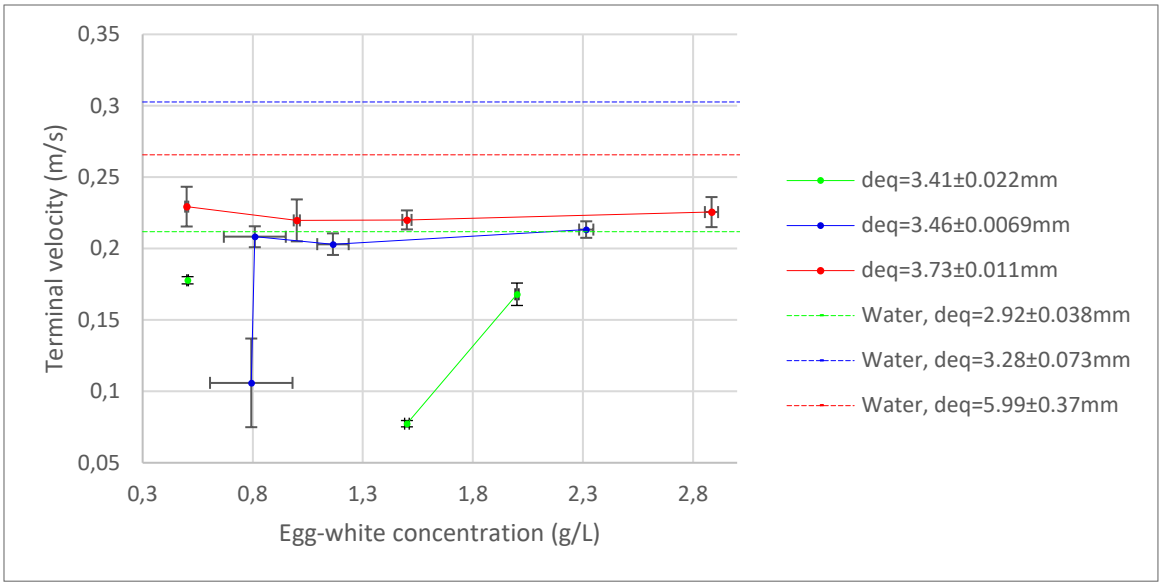

Figure 26 The terminal velocity with corresponding SEM for bubbles generated with the three selected combinations of capillary and volumetric flow rate in egg-white protein solutions with increasing concentration The calculated mean and SEM are based on the obtained data for a range of 3 to 90 bubbles.

The comparative analysis between the terminal velocities predicted with Eq. (7) and (8) and the experimentally derived terminal velocities of bubbles generated with the three selected combinations of capillary and volumetric flow rate in albumin and egg-white protein solutions with increasing concentration are represented in Fig. 27 and 28 below. The figures provide a projection of the accuracy of the equations in predicting the terminal velocity of bubbles rising in protein solutions. The relative small vertical error bars of both terminal velocity predictions by Clift and Fan and Tsuchiya illustrate that although there is some small uncertainty in the characteristics of the solutions such as the density, surface tension and the viscosity, both equations are able to give a specific prediction regarding the terminal velocity of bubbles rising through it. Analyzing the morphology of the graphs and datapoints, reveals the overprediction of the terminal velocity of bubbles rising in protein solutions by the equation of Fan and Tsuchiya by approximately 0.10m/s. On the contrary, the terminal velocity predictions by Clift of bubbles rising in albumin solutions approach the experimentally derived terminal velocities better. The terminal velocity predictions of bubbles generated with the capillary having the intermediate-sized inner diameter in egg-white protein solutions even equalize the experimentally derived terminal velocities. However, the predictions of Clift also tend to overpredict the terminal velocity of bubbles rising in albumin solutions and substantially overpredict the terminal velocity of bubbles generated with the capillaries having the smallest and largest inner diameter in egg-white protein solutions. The overprediction of the terminal velocity of bubbles rising in protein solutions, suggests the underestimation of the increased drag forces due to the higher viscosity and density of the fluid. Apart from that, the equation of Fan and Tsuchiya shows a decreasing trend while the equation of Clift shows an increasing trend in the terminal velocity of bubbles ascending in albumin solutions with increasing inner diameter of the capillary. However, Clift's prediction of the terminal velocity of bubbles rising in egg-white protein solutions show a substantial decrease when increasing the inner diameter of the capillary from 0.254 to 0.762mm upon a substantial increment when further increasing the inner diameter. Only the trend in the predictions of Clift for albumin solutions and the predictions of Fan and Tsuchiya for bubbles rising in approximately 1.04g/L egg-white solution agree the trend visible in the experimentally derived terminal velocities. Besides, only Clift's terminal velocity predictions of bubbles generated form the capillary having the intermediate-sized inner diameter in egg-white

solutions, represents differences between the varying concentrations that agree with the differences in the experimentally derived terminal velocity of bubbles rising in solutions with different protein concentration. All other terminal velocity predictions tend to be insensitive towards the differences in protein concentration.

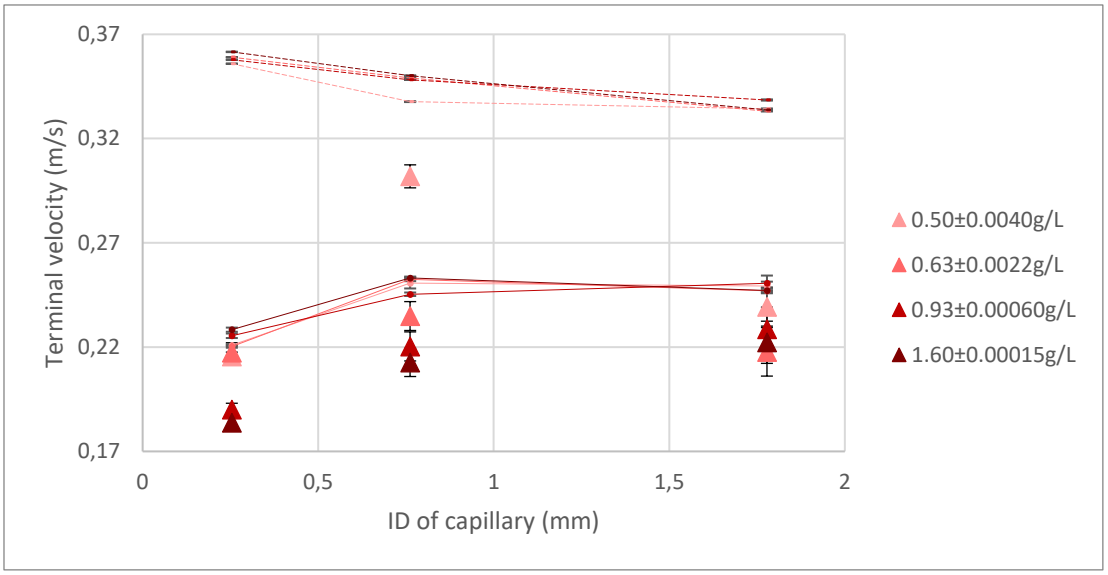

Figure 27 Comparison between the terminal velocity predicted with the equation of Fan and Tsuchiya (dotted graphs), with the equation of Clift (continuous graphs) and the experimentally derived terminal velocity (datapoints) for bubbles generated with the three selected combinations of capillary size and volumetric flow rate which rise in albumin solutions with increasing concentration represented in the legenda. Higher salt concentrations are visualized with darker colors in this figure. The calculated mean and SEM are based on the obtained data for a range of 5 to 69 bubbles.

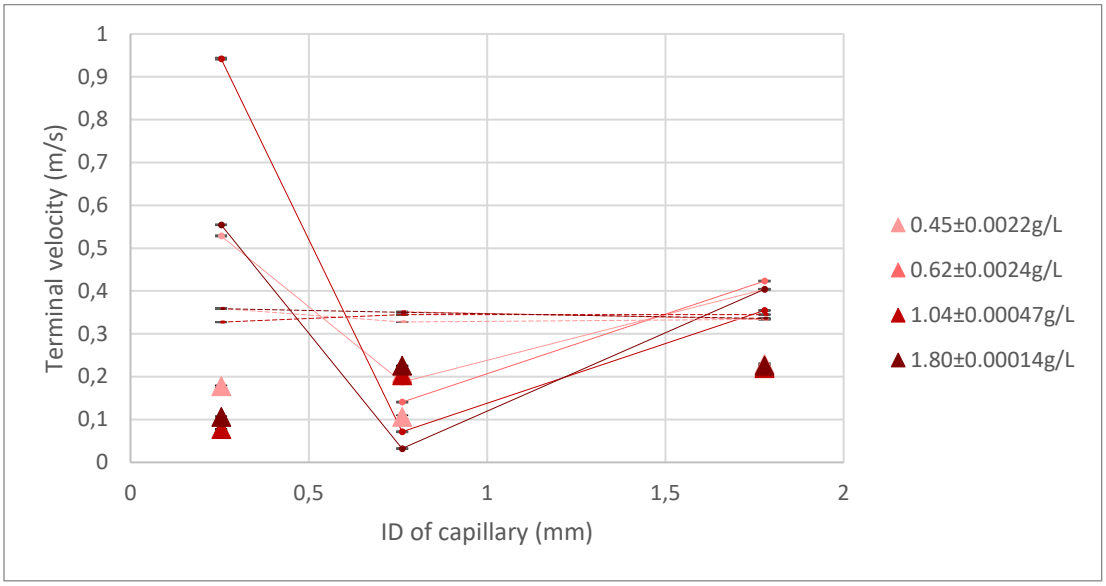

Figure 28 Comparison between the terminal velocity values predicted using the equation of Fan and Tsuchiya (dotted graphs), using the equation of Clift (continuous graphs) and the experimentally derived terminal velocity (datapoints) for bubbles generated with the three selected combinations of capillary size and volumetric flow rate which rise in egg-white solutions with increasing concentration represented in the legenda. Higher salt concentrations are visualized with darker colors in this figure. The calculated mean and SEM are based on the obtained data for a range of 3 to 90 bubbles.

The comparative analysis on the relationship between the drag coefficients predicted with Eq. (2) and (3) and the experimentally derived drag coefficients of bubbles generated with the three selected combinations of capillary and volumetric flow rate in protein solutions with increasing concentration are presented in Fig. 29 and 30 below. The figures provide a projection of the accuracy

of the models in predicting the drag coefficient of bubbles rising in protein solution. Firstly, the vertical error bars originating from the SEM associated with the calculated drag coefficients are negligible, stating bubbles with approximately the same equivalent diameter rising in protein solutions, exhibit the same drag coefficient. This is an indication that the formed bubbles with comparable equivalent diameter possess a consistent shape and are likely to have reached a uniform steady-state within the protein solutions which makes their behavior predictable. The horizontal error bars that become more prominent for bubbles rising in albumin solutions at high Re, are a result of bigger deviations in the larger equivalent diameter of bubbles ascending in albumin solutions, in the higher density of the albumin solutions as well as less deviation in the slightly lower viscosity compared to egg-white protein solutions. The grouping of the drag coefficient ratios per capillary in albumin solutions, stem from constant Re because of balanced changes in equivalent diameter and terminal velocity as represented in Fig. 23 and 24 . Furthermore, from the values of the represented ratios, it can be seen that the predictions of Ishii and Zuber converge to 1 between Re 600 and 800. This states that the predictions approach and almost equalize the experimentally derived drag coefficients within that Re interval. However, the equation tends to slightly underpredict the drag coefficient of bubbles rising in protein solutions at Re lower than 600 and slightly overpredict the drag coefficient at Re higher than 800. This suggests the slight overestimating of the drag force experienced by bigger bubbles while underestimating the effects for smaller bubbles when rising in protein solutions by the equation of Ishii and Zuber. On the contrary, the predictions from Peebles and Garber consistently underpredict the drag coefficients of bubbles rising in protein solutions with Re below 1000 that becomes more substantial at low Re. However, when combining both figures, convergence of the predictions by Peebles and Garber can be detected around Re 1000 while showing overprediction of the drag coefficient of bubbles rising in albumin solution with Re around 1050. This suggests substantial underestimation of the drag forces experienced by smaller bubbles while overestimating the effects for bigger bubbles when rising in protein solutions by the equation of Peebles and Garber.

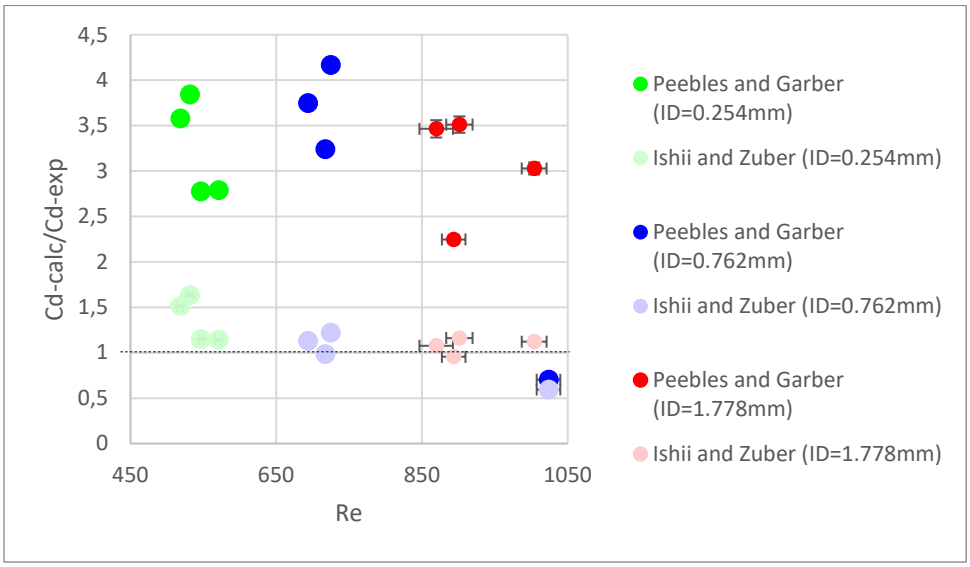

Figure 29 Ratio between the experimentally derived drag coefficient and drag coefficients predicted with the equations of Peebles and Garber and Ishii and Zuber (Eq. (2) and (3)) as a function of Re for bubbles generated with the three selected combinations of capillary and volumetric flow rate in albumin solutions with increasing concentration. The calculations are based on the obtained data for a range of 5 to 69 bubbles.

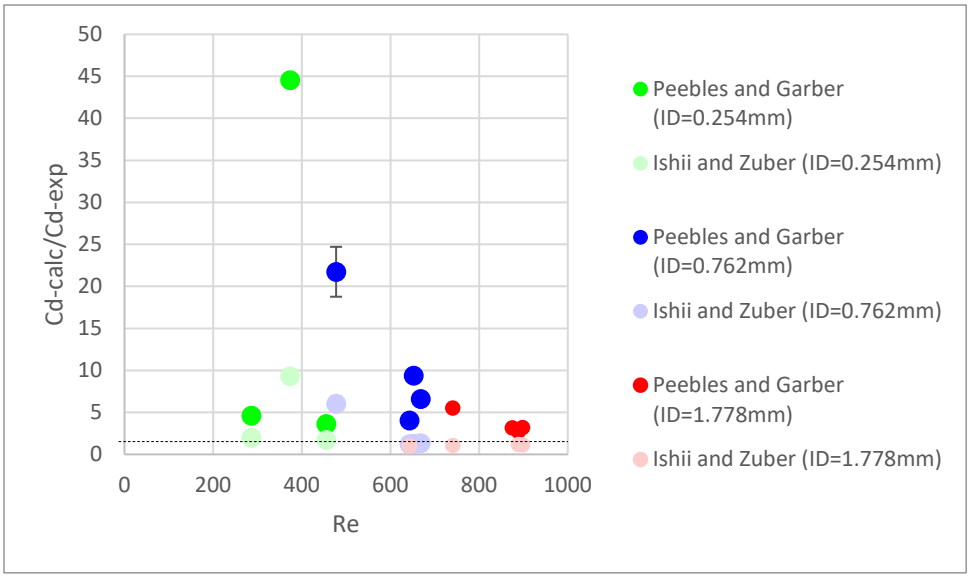

Figure 30 Ratio between the experimentally derived drag coefficient and drag coefficients predicted with the equations of Peebles and Garber and Ishii and Zuber (Eq. (2) and (3)) as a function of Re for bubbles generated with the three selected combinations of capillary and volumetric flow rate in egg-white solutions with increasing concentration. The calculations are based on the obtained data for a range of 3 to 90 bubbles.

4.4 Comparative analysis on drag coefficient of single bubbles rising in salt and protein solutions

The drag coefficient predictions and the experimentally derived drag coefficients of bubbles generated with the three selected combinations of capillary and volumetric flow rate when rising in demineralized water and the NaCl, Na2SO4, albumin and egg-white protein solutions with varying concentrations are represented in Fig. 31 and 32 below. The figures provide a projection of the influence of salt and protein on the drag coefficient of bubbles rising through the solution. In Fig. 31 it can be seen that more datapoints regarding bubbles rising in salt solutions are situated below the experimentally derived drag coefficient of bubbles ascending in demineralized water between Re 900 and 1000, while almost all datapoints are situated above the experimentally derived drag coefficient of bubbles ascending in demineralized water from Re 1000 to 1100. This suggests a slight decrease in the drag coefficient of smaller bubbles and an increase in the drag coefficient of bigger bubbles. In Fig. 32 a slight increment of the drag coefficient of bubbles rising in protein solution with Re around 600 is visible while the drag coefficient of bubbles with Re around 1000 shows a more substantial increase. This suggest small bubbles rising in salt solutions experience less drag force while bigger bubbles ascending in salt solutions and bubbles rising in protein solutions experience a stronger drag force.

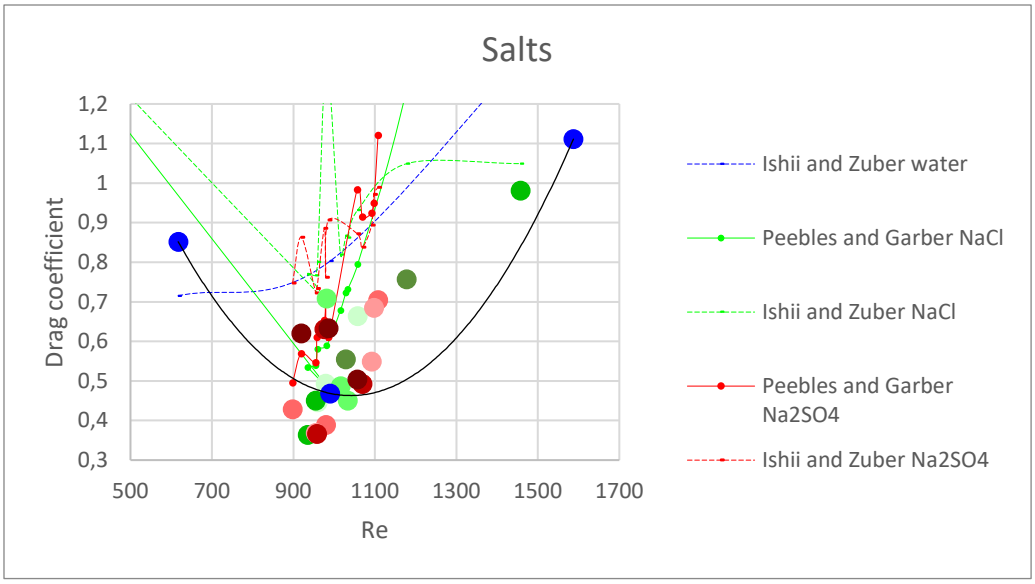

Figure 31 The experimentally derived drag coefficients and the drag coefficients predicted with the equations of Peebles and Garber and Ishii and Zuber (Eq. (2) and (3)) as a function of Re for bubbles generated with the three selected combinations of capillary and volumetric flow rate in salt solutions with increasing concentration. Higher concentrations are represented with darker colors.

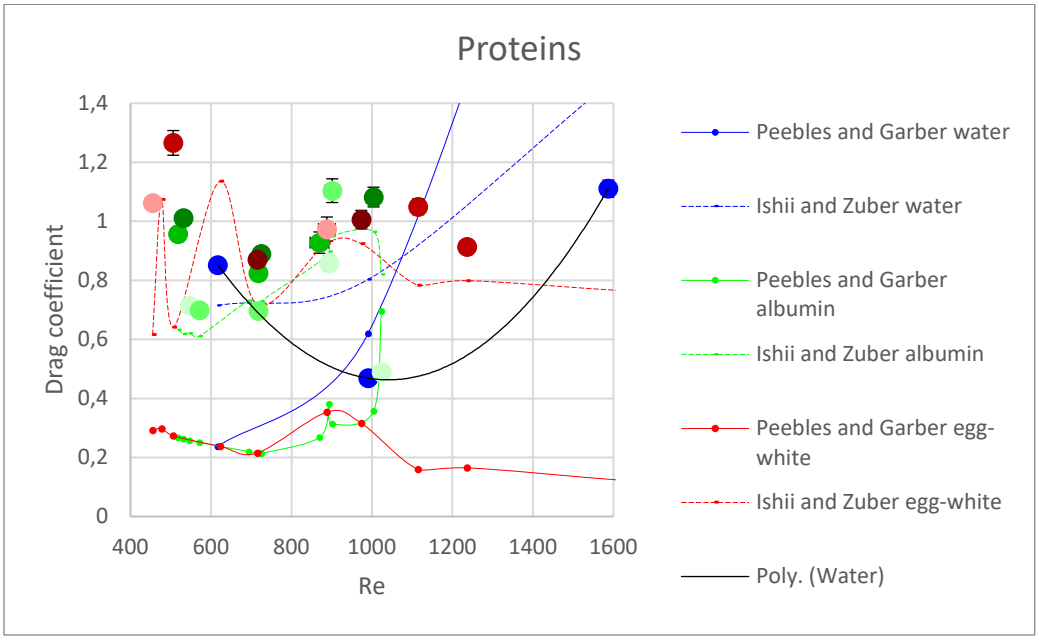

Figure 32 The experimentally derived drag coefficients and the drag coefficients predicted with the equations of Peebles and Garber and Ishii and Zuber (Eq. (2) and (3)) as a function of Re for bubbles generated with the three selected combinations of capillary and volumetric flow rate in protein solutions with increasing concentration. Higher concentrations are represented with darker colors.

4.5 Equivalent diameter predictions

Combining the comparative analysis between the equivalent diameters predicted with Eq. (11) and the experimentally derived equivalent diameters of bubbles generated with the three selected combinations of capillary and volumetric flow rate in demineralized water and the NaCl, Na2SO4, albumin and egg-white protein solutions with the highest experimented concentration results in Fig. 33 below. The figure provides a projection of the accuracy of the equation in predicting the equivalent diameter of bubbles rising in varying solutions. The relative small vertical error bars illustrate that all capillaries are consistently predicted to generate bubbles with a uniform equivalent

diameter. Analyzing the morphology of the graphs reveals that the presence of the specific salts present in concentrations lower than approximately 0.23mol/L as well as the presence of albumin and egg-white protein in concentrations lower than approximately 1.80g/L are predicted to have little effect on the equivalent diameter of bubbles rising through the solution. This contradicts the more visible differences in the experimentally derived equivalent diameter of bubbles ascending in the different solutions. Moreover, the equation slightly underpredicts the equivalent diameter of bubbles generated with the two capillaries having the smallest inner diameter while it tends to slightly overpredict the equivalent diameter of bubbles generated with the capillary with the largest inner diameter regarding the salt and protein solutions. The equivalent diameter of bubbles generated with the capillary having the largest inner diameter in demineralized water is an exception in this trend and is underpredicted by the equation. These specific bubbles were observed to be the most deformable, further represented by the larger vertical error bar. The equivalent diameter seems to be in agreement with the observed bubble size which suggests that the equation might not give accurate predictions of the equivalent bubble diameter of deformable bubbles. This trend of slight overarching for a capillary inner diameter smaller than 0.762mm and slight under arching for bigger capillary inner diameter while approaching the experimental results for the capillary having inner diameter 0.762mm, suggests a insensitivity to capillary-size dependent effects. The geometry of the capillary determined by the combination of inner and outer diameter, lead to different entrance effects. The capillary having inner diameter 0.254mm and a broader outer diameter can enable an increased curvature of the liquid-air interface which can enhance surface tension effects. Together with the wider wetted area, the formation of somewhat bigger bubbles can be promoted. The relatively small outer diameter of the capillary having inner diameter 1.778mm may result therefore in slightly smaller bubbles than expected when neglecting the capillary effects.

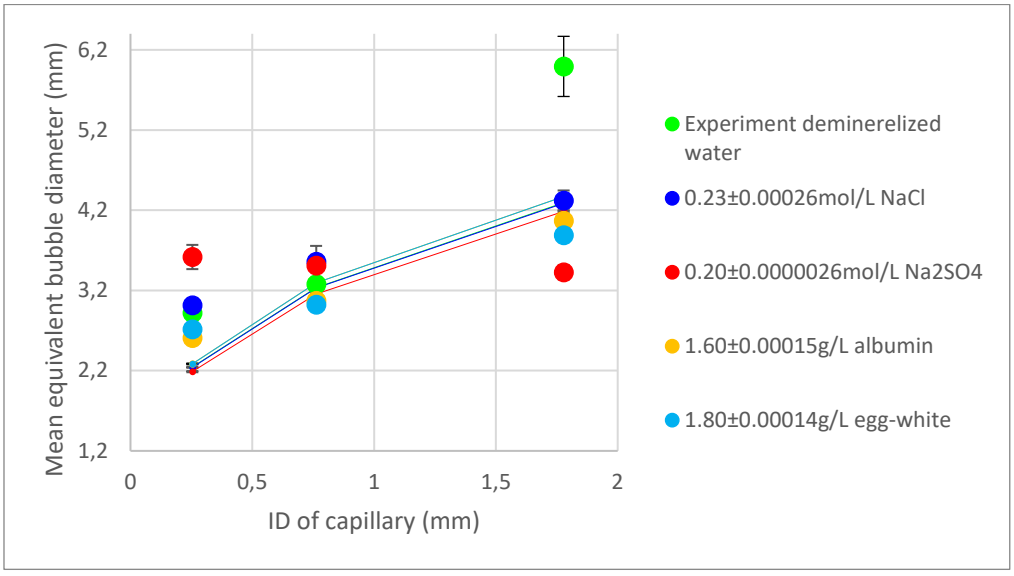

Figure 33 Comparison between bubble equivalent diameters predicted using Eq. (11) (continuous graphs) and experimental bubble equivalent diameters (datapoints) for bubbles generated with the three selected combinations of capillary size and volumetric flow rate which rise in demineralized water, salt and protein solutions with the highest concentration studied, represented in the legenda.

5

Conclusion

The addition of salts in demineralized water led to a higher density of the fluid. The presence of NaCl and Na2SO4 in demineralized water tend to reduce the equivalent diameter of bubbles with an initial equivalent diameter of approximately 6.00mm. This effect is more pronounced for Na2SO4, leading to a reduction in bubble size by up to one third. This goes together with a slight increase in their terminal velocity. The addition of salts is almost non-influential to the equivalent diameter of bubbles with an initial equivalent diameter of approximately 3.00mm while tending to slightly enlarge smaller bubbles. The terminal velocity of these slightly growing bubbles increases. Overall, bubbles rising in salt solutions exhibited a smaller size distribution compared to demineralized water. This shrinking of bigger bubbles indicates that the drag force becomes more dominant due to the increment in the fluid's density. This together with the slight enlargement of smaller bubbles is confirmed by the decrease in the drag coefficient for bubbles with Re lower than 1000 while increasing drag coefficients are shown for higher Re. This increasing drag force is expected to become somewhat more pronounced upon increasing the salt concentration, as is suggested by the tendence of the terminal velocities to slightly decrease. Furthermore, the presence of NaCl and Na2SO4 from concentrations of approximately 0.075mol/L on, reduce the oscillation in the terminal velocity of the ascending bubbles with equal amounts when compared to the terminal bubble velocities in demineralized water. Further increasing the salt concentrations is thought to have little effect on the oscillation of the terminal velocity of single rising bubbles. The equation of Fan and Tsuchiya tends to overpredict the terminal velocity of bubbles rising in salt solutions. On the contrary, the equation of Clift consistently underpredicts the terminal velocity of bubbles rising in salt solutions. This suggests the equation of Fan and Tsuchiya underestimates the increased drag force while the equation of Clift is likely to overestimate the effects of the increased drag forces experienced by bubbles ascending in salt solutions. However, both equations are able to capture the overall trend in the terminal velocity and the equation of Fan and Tsuchiya does represents the deviations in the terminal velocity of bubbles rising in solutions with varying concentrations well. Furthermore, bubbles rising in the salt solutions showed a more ellipsoidal shape and substantial deformability with increasing bubble size, resulting in wobbling bubbles and dimpled ellipsoidal bubbles with the dimple on top. The drag models of Ishii and Zuber and Peebles and Garber consistently underpredict the drag coefficient of bubbles rising in salt solutions. This can be attributed to missing incorporated bubble deformability in both models. Overall, the predictions of Peebles and Garber approach the experimentally derived drag coefficients around Re 1000 while the predictions by Ishii and Zuber tend to more accurately predict the drag coefficient around Re 1500.

The addition of proteins in demineralized water led to a higher density and viscosity of the fluid. The presence of albumin and egg-white in demineralized water tend to reduce the equivalent diameter of bubbles with an initial equivalent diameter of approximately 6.00mm by one third, aligning with the effects of salts present. The reduction in bubble size can be attributed to the increased fluid's density. The reduction in their terminal velocity, indicates the increased viscous drag effects because of the present proteins. The addition of proteins is almost non-influential to the equivalent diameter of bubbles with an initial equivalent diameter of approximately 3.00mm. However, egg-white tends to enlarge bubbles with an initial equivalent diameter smaller than 3.00mm. This agrees with the effect of salts and suggests the possible presence of salts form egg-white in the protein powder. This goes together with a reduction of their terminal velocity. This higher terminal velocity reached by the larger bubbles can be attributed to their bigger momentum overcoming the increased resistance to flow because of the enlarged viscosity of the fluid. Further increasing the protein concentrations from around 0.50g/L on, has little effect on the equivalent diameter and the terminal velocity of single rising bubbles. This suggests that the increasing density and viscosity lead to an equal ratio between drag and Buoyancy forces. Overall, bubbles rising in protein solutions exhibited a smaller size distribution compared to demineralized water, with slightly smaller equivalent diameters favored in comparison to bubbles ascending in salt solutions. The reduction in the terminal velocity is confirmed by the slight increase in the drag coefficient of the bubbles. Also, the similar terminal velocities are represented in the drag coefficients with equal magnitude. Furthermore, the terminal velocity of bubbles rising in protein solutions is slightly smaller than in salt solutions. The terminal velocities exhibit oscillation within the same magnitude, although slightly decreasing upon increasing of the protein concentration. Both the equation of Fan and Tsuchiya and Clift overpredict the terminal velocity of bubbles rising in protein solutions. However, the equation of Clift is able to capture the trend in the terminal velocity in albumin solutions while the equation of Fan and Tsuchiya follows the trend in egg-white solutions better. Furthermore, bubbles rising in the protein solutions showed a more spherical shape and slight deformability with increasing bubble size which resulted in more ellipsoidal bubble shapes. The drag coefficient predictions of Ishii and Zuber are in accordance to the experimentally derived drag coefficients between Re 600 and 800 while slightly underpredicting at lower Re. However, the drag model of Peebles and Garber consistently underpredicts the drag coefficient of bubbles rising in protein solutions with Re lower than 1000. This underprediction of the drag coefficients suggests the underestimation of the drag force. This suggests both models interpret the influence of the increased viscosity wrong. Overall, the predictions of Ishii and Zuber give accurate drag coefficient predictions with Re lower than 1000 while the predictions by Peebles and Garber tend to more accurately predict the drag coefficient from Re 1000.

Furthermore, Eq. (11) is able to give accurate predictions of the equivalent bubble diameter when rising in the salt and protein solutions. However, the slight underpredicting of the equivalent diameters of bubbles generated with the capillary having the smallest inner diameter confirm the indication of an insensitivity to capillary-size dependent effects as stated in the comparison with the equivalent bubble diameters in demineralized water. Moreover, the slight overpredicting of the equivalent diameters of bubbles generated with the capillary having the largest inner diameter represent the effect of the missing viscosity term.

To conclude, both salts and proteins have a shrinking effect on bigger bubbles while slightly enlarging smaller bubbles, resulting in a more narrow bubble size distribution in comparison with demineralized water. Furthermore, the presence of these surfactants reinforce the drag force experienced by the single rising bubbles. For the salt solutions, this can be attributed to the increased density of the fluid while the increment in the fluid's viscosity is influential in protein solutions. the

drag model of Ishii and Zuber is able to predict the drag coefficients of bubbles rising in protein solutions while the drag model of Peebles and Garber is more in accordance with the experimental results of bubbles rising in salt solutions. This increment in the drag coefficient together with the smaller bubble sizes and lower terminal velocities of bubbles rising in salt and protein solutions suggests more gas hold-up and hereby a potential increase in the gas-liquid mass transfer.

6

Recommendations

In the experimental phase, certain recommendations for execution are noted. To begin with, the preparation of the solutions involved the use of beaker glasses to measure demineralized water. For further research a weighing scale is recommended to reduce the deviations in volume. Such improvements are crucial as they impact the computed density and concentration, which are integrated in Eo, Mo, We, and Re. These, in turn, have a direct influence on the predictions of terminal velocity and drag coefficient. Additionally, for consistency and ease of correlation between data points, it is suggested to prepare larger quantities of solutions in advance to ensure that measurements are conducted under the same concentration conditions. Apart from that, measuring the viscosity of the salt solutions would further refine the accuracy of the calculations. The measured surface tension of the protein solutions exceeds that of demineralized water, while the surface tension of the Na2SO4 solution is lower, in contrast to the excepted. This discrepancy is likely attributed to potential inaccuracies in calibrating the BPT mobile with respect to the surface tension of demineralized water. Moreover, to enhance the reliability of surface tension measurements for the 2.00g/L egg-white solution, it is advisable to extend the surface age during measurement to approach convergence towards a stable value. Furthermore, experimenting with the combinations of capillary and volumetric flow rate to generate more divergent bubble sizes would be interesting. Potential studies with a broader bubble size distribution would expand the range of Reynolds numbers, providing data for a more complete understanding of the effects of salts and proteins on the drag coefficient of single rising bubbles. Moreover, it would be intriguing to investigate the impact of additional salts and proteins commonly found in biochemical broths, such as NH2Cl and (NH4)2SO4. Comprehensive measurements, incorporating the combination of surfactants, could provide further insights into their influence on the drag coefficient of bubbles rising in broth. This study would then also examine the interactions between surfactants, contributing to a more comprehensive understanding of the system.

Regarding the data acquisition, it is recommended to assess the software's performance by comparing its outcomes with those of another software, rather than relying solely on manual measurements conducted using ImageJ. Also, employing a camera with higher resolution could enhance the software's ability to capture bubbles with greater precision due to sharper contours. This would be especially favorable for the cloudy protein solutions. Besides, further refining the software's tuning for each unique dataset, could enhance the results due to the potential detection of a greater number of bubbles and the possible improvement of the accuracy of the bubble capturing. Additionally, it is recommended to develop a code that can systematically process the data acquired by the software. This code should encompass functionalities such as computing the mean equivalent bubble diameter with its corresponding SEM for with usable bubble detections, identifying the steady-state regime, calculating the terminal velocity within this interval and providing the number of bubbles considered in the calculations. Within this code, a function capable of computing the predicted equivalent bubble diameter, terminal velocity and calculated and predicted drag coefficients upon importing the requisite parameters, could be created. Lastly, it is

recommended to conduct a more in-depth analysis of the velocity profiles of individual rising bubbles. This could involve, for instance, plotting Fourier transformations through the data points. Such an approach has the potential to enhance the understanding of bubble behavior in salt and protein solutions.

It must be noted that the terminal velocity predictions by Fan and Tsuchiya were done with the Kb of pure systems because it showed, as represented in the appendix, even more overpredicting with the Kb of contaminated systems. This suggests the Kb for contaminated systems is more related to higher concentrated solutions. These constants need further examination. Concerning the predictive equations and models, it would be advantageous to expand the number of bubbles included in the calculations to assess the accuracy of results that are now based on limited bubbles. If it turns out the experimentally derived values do effectively represent observed phenomena, adjustments to the predicting equations of the equivalent bubble diameter, the equations by Clift and Fan and Tsuchiya and the drag models of Peebles and Garber and Ishii and Zuber should be adjusted. For instance, it is recommended to incorporate the influence of outer diameter on bubble sizes in the equation predicting the equivalent bubble diameter. Additionally, adjustments should be made to incorporate the experienced drag force by single bubbles rising in surfactant solutions in the terminal velocity predictions by Clift and Fan and Tsuchiya. Furthermore, the drag models should account for bubble deformability. Finally, the effects of increased viscosity should be considered in the model of Peebles and Garber. In addition to enhancing the investigated equations and models, it is advised to first evaluate the predictive capabilities of alternative relationships. Examples of drag models and terminal velocity predicting equations for contaminated systems are provided in Table 3 and 4 below.

Drag models			
$C_D = max\left\{\min\left(\frac{24}{Re}(1+0.15Re^{0.678}), \frac{72}{Re}\right), \frac{8}{3}\frac{Eo}{Eo+4}\right\}$	(5)	Tomiyama et al.	Contaminated system Applicable range: $10^{-2} < Eo < 10^{3}$ $10^{-3} < Re < 10^{5}$ $10^{-14} < Mo < 10^{7}$
$C_D = \frac{16}{Re}\begin{bmatrix}(\frac{1}{2}+32\theta+\frac{1}{2}\sqrt{1+128\theta})^{\frac{1}{3}} \\ +(\frac{1}{2}+32\theta-\frac{1}{2}\sqrt{1+128\theta})^{\frac{1}{3}} \\ +(0.036(\frac{128}{3})^{\frac{1}{9}}Re^{\frac{8}{9}}Mo^{\frac{1}{9}}\end{bmatrix}$	(6)	Rodrigue	
$C_D = \left[(C_{D,Mei})^2 + (C_D(Eo))^2\right]^{0.5}$ $C_{D,Mei} = \frac{16}{Re}\left\{1+\left[\frac{8}{Re}+\frac{1}{2}(1+\frac{3.315}{Re^{0.5}})\right]^{-1}\right\}$ $C_D(Eo) = max\left\{10^{-1.23\log(Eo)+0.37\log(Mo)+1.6}, min\left[\frac{4Eo}{Eo+9.5}, \frac{8}{3}\frac{Eo}{0.8762Eo+4.8}\right.\right.$	(7)	Zhou et al.	Pure and contaminated system Applicable range: $10^{-2} < Eo < 10^{-3}$ $10^{-3} < Re < 10^{5}$

			10^{-14} < Mo < 10^{7}
$C_D = max\left\{\min\left(\frac{24}{Re}(1+0.15Re^{0.678}), \frac{72}{Re}\right), \frac{24}{Re}(1 + 0.15Re^{0.678})\frac{Re^{0.55}Eo^{0.95}We^{-1.10}}{12.6}\left(\frac{Mo}{Mo^*}\right)^{0.048}\right\}$ $Mo^* = 2.6x10^{-11}$	(8)	Yan et al.	Pure and contaminated system Applicable range: 10^{-2} < Eo < 10^{3} 10^{-3} < Re < 10^{6} 10^{-14} < Mo < 10^{7}
$C_D = \begin{cases} \frac{24(1+0.15Re^{0.687})}{Re}, Re \le 1000 \\ 0.44, Re > 1000 \end{cases}$	(2)	Schiller and Naumann	

Table 3 Drag models.

Terminal velocity equations			
$v_T^{stokes} = \frac{1}{18}\frac{g{d_{eq}}^2(\rho_l - \rho_g)}{\mu_l}$	(8)	Stokes	Small spherical bubbles
$v_T^{Clift} = \frac{\mu_L}{\rho_L d_{eq}} Mo^{-0.149}(J - 0.857)$	(9)	Clift	Bubble in contaminated system
$v_T^{Mendelson} = \sqrt{\frac{2\sigma}{d_{eq}(\rho_l+\rho_g)} + \frac{gd_{eq}}{2}}$	(10)	Mendelson	Spherical bubbles with diameter >1.3mm
$v_T^{Jam} = \frac{v_T^{stokes} v_T^{Mendelson}}{\sqrt{(v_T^{stokes})^2 (v_T^{Mendelson})^2}}$	(11)	Jamialahmadi et al.	
$v_T^{FT} = (v_{T1}^{-n} + v_{T2}^{-n})^{-\frac{1}{n}}$ $v_{T1} = \frac{\rho_l}{K_b \mu_l} g{d_b}^2$ $v_{T2} = \sqrt{\frac{2q\sigma}{d_{eq}(\rho_l+\rho_b)} + \frac{(\rho_l - \rho_b)gd_{eq}}{2\rho}}$ $K_b = \max(12, K_{bo}Mo^{-0.038})$	(12)	Fan and Tsuchiya	Bubble in pure or contaminated system In pure system, $K_{bo} = 14.7$ and $n = 1.6$ In contaminated system, $K_{bo} = 10.2$ and $n = 0.8$ In compressible liquid, $q = 1.4$; otherwise, $q = 1.2$
$v_T^Z = (v_{T1}^{-1.31} + v_{T2}^{-1.31})^{-\frac{1}{1.31}}$ $v_{T1} = \frac{\rho_l}{K_b \mu_l} g{d_{eq}}^2$ $K_b = \max(12, K_{bo}Mo^{-0.038})$ $v_{T2} = \frac{sin^{-1}\sqrt{1-E^2} - E\sqrt{1-E^2}}{1-E^2} \cdot \sqrt{0.92 \cdot \frac{8\sigma}{\rho_l d_b} E^{\frac{4}{3}} + 2.75 \cdot \frac{(\rho_l - \rho_g)gd_b}{2\rho_l}\frac{E^{\frac{2}{3}}}{1-E^2}}$ $E = aspect\ ratio\ of\ bubble$	(13)	Zheng et al.	Bubble in contaminated system Applicable range: $0.04 < Eo < 91.16$ $0.08 < Re < 1062$ $3.29 \times 10\ 11 < Mo < 4.29$

Table 4 Terminal velocity equations.

References

[1] F. J. Montes, M. A. Galan, and R. L. Cerro, 'Mass transfer from oscillating bubbles in bioreactors', *Chem. Eng. Sci.*, vol. 54, no. 15–16, pp. 3127–3136, Jul. 1999, doi: 10.1016/S0009-2509(98)00314-5.

[2] 'Bioreactors: Design and Operation'.

[3] N. Kantarci, F. Borak, and K. O. Ulgen, 'Bubble column reactors', *Process Biochem.*, vol. 40, no. 7, pp. 2263–2283, Jun. 2005, doi: 10.1016/j.procbio.2004.10.004.

[4] M. A. R. Talaia, 'Terminal Velocity of a Bubble Rise in a Liquid Column', vol. 1, no. 4, 2007.

[5] E. Delnoij, J. A. M. Kuipers, and W. P. M. Van Swaaij, 'Computational fluid dynamics applied to gas-liquid contactors', *Chem. Eng. Sci.*, vol. 52, no. 21–22, pp. 3623–3638, Nov. 1997, doi: 10.1016/S0009-2509(97)00268-6.

[6] L. Puiman, M. P. Elisiário, L. M. L. Crasborn, L. E. C. H. Wagenaar, A. J. J. Straathof, and C. Haringa, 'Gas mass transfer in syngas fermentation broths is enhanced by ethanol', *Biochem. Eng. J.*, vol. 185, p. 108505, Jul. 2022, doi: 10.1016/j.bej.2022.108505.

[7] 'Drag Coefficient Prediction of a Single Bubble Rising in Liquids'.

[8] K. Ekambara and M. T. Dhotre, 'CFD simulation of bubble column', *Nucl. Eng. Des.*, vol. 240, no. 5, pp. 963–969, May 2010, doi: 10.1016/j.nucengdes.2010.01.016.

[9] A. Sam, C. O. Gomez, and J. A. Finch, 'Axial velocity profiles of single bubbles in water/frother solutions', *Int. J. Miner. Process.*, vol. 47, no. 3–4, pp. 177–196, Aug. 1996, doi: 10.1016/0301-7516(95)00088-7.

[10] 'Design Parameters Estimations for Bubble Column Reactors'.

[11] M. Pourtousi, J. N. Sahu, and P. Ganesan, 'Effect of interfacial forces and turbulence models on predicting flow pattern inside the bubble column', *Chem. Eng. Process. Process Intensif.*, vol. 75, pp. 38–47, Jan. 2014, doi: 10.1016/j.cep.2013.11.001.

[12] M. K. Silva, M. A. d'Ávila, and M. Mori, 'Study of the interfacial forces and turbulence models in a bubble column', *Comput. Chem. Eng.*, vol. 44, pp. 34–44, Sep. 2012, doi: 10.1016/j.compchemeng.2012.04.007.

[13] E. Ertekin, J. M. Kavanagh, D. F. Fletcher, and D. D. McClure, 'Validation studies to assist in the development of scale and system independent CFD models for industrial bubble columns', *Chem. Eng. Res. Des.*, vol. 171, pp. 1–12, Jul. 2021, doi: 10.1016/j.cherd.2021.04.023.

[14] M. V. Tabib, S. A. Roy, and J. B. Joshi, 'CFD simulation of bubble column—An analysis of interphase forces and turbulence models', *Chem. Eng. J.*, vol. 139, no. 3, pp. 589–614, Jun. 2008, doi: 10.1016/j.cej.2007.09.015.

[15] H. D. Goodfellow and E. F. Curd, 'Physical fundamentals', in *Industrial Ventilation Design Guidebook*, Elsevier, 2020, pp. 39–109. doi: 10.1016/B978-0-12-816780-9.00004-6.

[16] P. Wang, J. J. Cilliers, S. J. Neethling, and P. R. Brito-Parada, 'The behavior of rising bubbles covered by particles', *Chem. Eng. J.*, vol. 365, pp. 111–120, Jun. 2019, doi: 10.1016/j.cej.2019.02.005.

[17] D. Wang and L.-S. Fan, 'Particle characterization and behavior relevant to fluidized bed combustion and gasification systems', in *Fluidized Bed Technologies for Near-Zero Emission Combustion and Gasification*, Elsevier, 2013, pp. 42–76. doi: 10.1533/9780857098801.1.42.

[18] L. Liu, H. Yan, and G. Zhao, 'Experimental studies on the shape and motion of air bubbles in viscous liquids', *Exp. Therm. Fluid Sci.*, vol. 62, pp. 109–121, Apr. 2015, doi: 10.1016/j.expthermflusci.2014.11.018.

[19] J. B. Joshi, 'Computational ow modelling and design of bubble column reactors', *Chem. Eng. Sci.*, 2001.

[20] S. Maxemow, 'That's a Drag: The Effects of Drag Forces', *Undergrad. J. Math. Model. One Two*, vol. 2, no. 1, May 2013, doi: 10.5038/2326-3652.2.1.4.

[21] 'Buoyancy Force - an overview | ScienceDirect Topics'. Accessed: Sep. 11, 2023. [Online]. Available: https://www-sciencedirect-com.tudelft.idm.oclc.org/topics/engineering/buoyancy-force
[22] W. H. Ahmed, M. A. El-Nakla, and B. I. Ismail, 'Towards understanding the critical heat flux for industrial applications', *Int. J. Multiph. Flow*, vol. 36, no. 3, pp. 153–165, Mar. 2010, doi: 10.1016/j.ijmultiphaseflow.2009.10.002.
[23] C. T. Crowe, J. D. Schwarzkopf, M. Sommerfeld, and Y. Tsuji, *Multiphase Flows with Droplets and Particles, Second Edition*. CRC Press, 2011.
[24] 'The added mass, Basset, and viscous drag coefficients in nondilute bubbly liquids undergoing small-amplitude oscillatory motion'.
[25] N. Arden and M. J. Betenbaugh, 'Life and death in mammalian cell culture: strategies for apoptosis inhibition', *Trends Biotechnol.*, vol. 22, no. 4, pp. 174–180, Apr. 2004, doi: 10.1016/j.tibtech.2004.02.004.
[26] S. Hubalek, M. J. Post, and P. Moutsatsou, 'Towards resource-efficient and cost-efficient cultured meat', *Curr. Opin. Food Sci.*, vol. 47, p. 100885, Oct. 2022, doi: 10.1016/j.cofs.2022.100885.
[27] X. Sun, H. K. Atiyeh, R. L. Huhnke, and R. S. Tanner, 'Syngas fermentation process development for production of biofuels and chemicals: A review', *Bioresour. Technol. Rep.*, vol. 7, p. 100279, Sep. 2019, doi: 10.1016/j.biteb.2019.100279.
[28] G. Bozzano and M. Dente, 'Shape and terminal velocity of single bubble motion: a novel approach', *Comput. Chem. Eng.*, 2001.
[29] A. Prins and K. Van'T Riet, 'Proteins and surface effects in fermentation: foam, antifoam and mass transfer', *Trends Biotechnol.*, vol. 5, no. 11, pp. 296–301, Nov. 1987, doi: 10.1016/0167-7799(87)90080-1.
[30] J. H. Johnston, 'The Surface Tension of Protein Solutions. Part III', *Biochem. J.*, vol. 21, no. 6, pp. 1314–1328, 1927.
[31] 'Cradle to production gate life cycle assesment of cultured meat growth media:A comparison of Essential 8TM and Beefy-9'.
[32] 'Simple and effective serum-free medium for sustained expansion of bovine satellite cells for cell cultured meat'.
[33] Y. Zhou, C. Zhao, and H. Bo, 'Analyses and modified models for bubble shape and drag coefficient covering a wide range of working conditions', *Int. J. Multiph. Flow*, vol. 127, p. 103265, Jun. 2020, doi: 10.1016/j.ijmultiphaseflow.2020.103265.
[34] R. Prichard, M. Gibson, C. Joseph, and W. Strasser, 'A review of fluid flow in and around the brain, modeling, and abnormalities', in *Multiscale Biomechanical Modeling of the Brain*, Elsevier, 2022, pp. 209–238. doi: 10.1016/B978-0-12-818144-7.00015-3.
[35] B. E. Rapp, 'Fluids', in *Microfluidics: Modelling, Mechanics and Mathematics*, Elsevier, 2017, pp. 243–263. doi: 10.1016/B978-1-4557-3141-1.50009-5.
[36] X. Yan, Y. Jia, L. Wang, and Y. Cao, 'Drag coefficient fluctuation prediction of a single bubble rising in water', *Chem. Eng. J.*, vol. 316, pp. 553–562, May 2017, doi: 10.1016/j.cej.2017.01.137.
[37] R. Clift, J. R. Grace, and M. E. Weber, *Bubbles, Drops, and Particles*. Courier Corporation, 2005.
[38] 'Capillary Radius and Surface Tensions'.
[39] S. D. Lubetkin, 'The fundamentals of bubble evolution', *Chem. Soc. Rev.*, vol. 24, no. 4, p. 243, 1995, doi: 10.1039/cs9952400243.
[40] A. Smolianski, H. Haario, and P. Luukka, 'Vortex shedding behind a rising bubble and two-bubble coalescence: A numerical approach', *Appl. Math. Model.*, vol. 29, no. 7, pp. 615–632, Jul. 2005, doi: 10.1016/j.apm.2004.09.017.
[41] W. L. Haberman and R. K. Morton, 'AN EXPERIMENTAL INVESTIGATION OF THE DRAG AND SHAPE OF AIR BUBBLES RISING IN VARIOUS LIQUIDS'.

Appendices

A

Surface tension measurements

A.1 Surface tension measurements

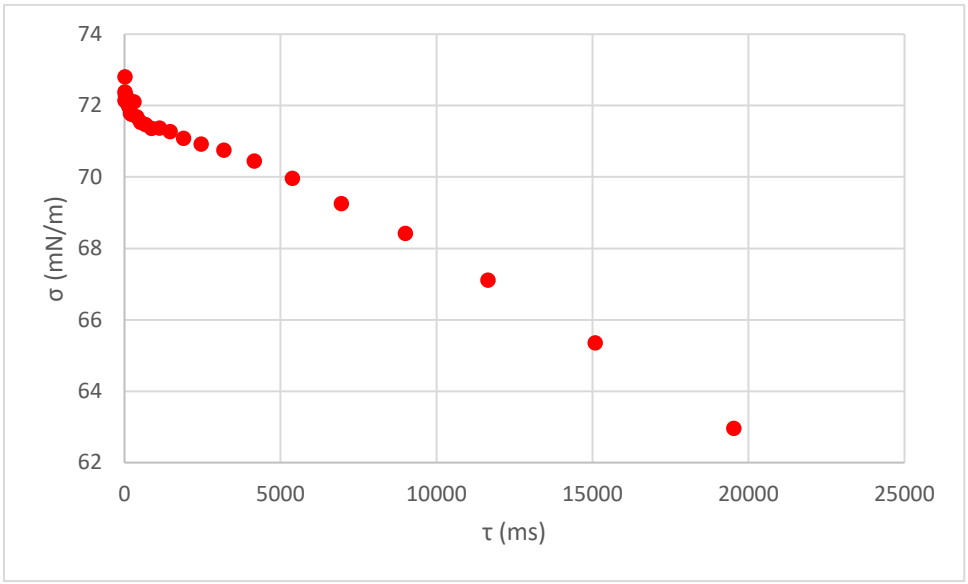

Figure 34 Result of the surface tension measurement of a 0.300mol/L Na2SO4 solution as a function of the surface age.

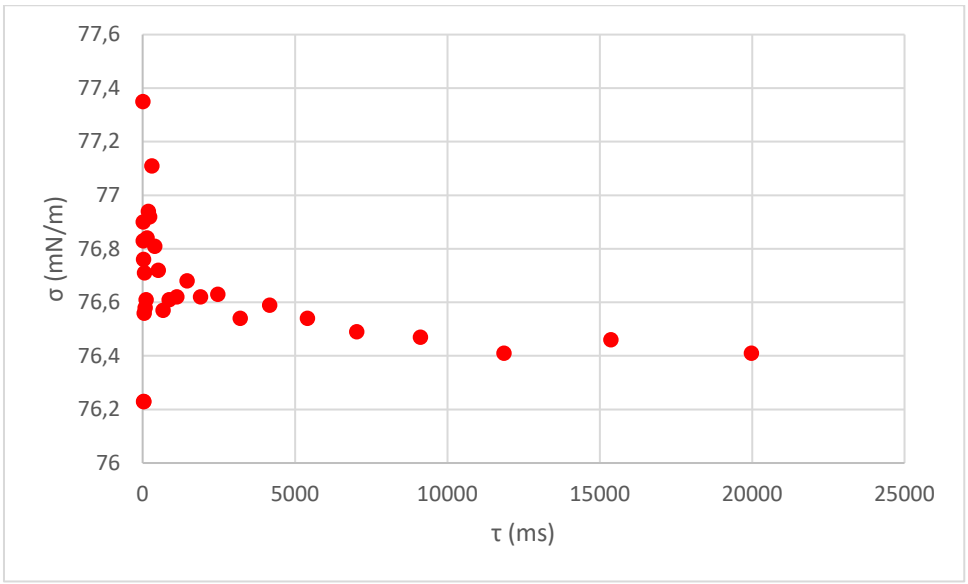

Figure 35 Result of the surface tension measurement of a 2.00g/L egg-white protein solution as a function of the surface age.

A.2 Viscosity values

2.00g/L Albumin solution	2.00g/L egg-white solution
1.060 mm^2/s	1.082 mm^2/s

Tabel 4 The kinemetic viscosity of albumin and egg-white solutions with 2.00g/L concentration.

B

Velocity and equivalent diameter profiles

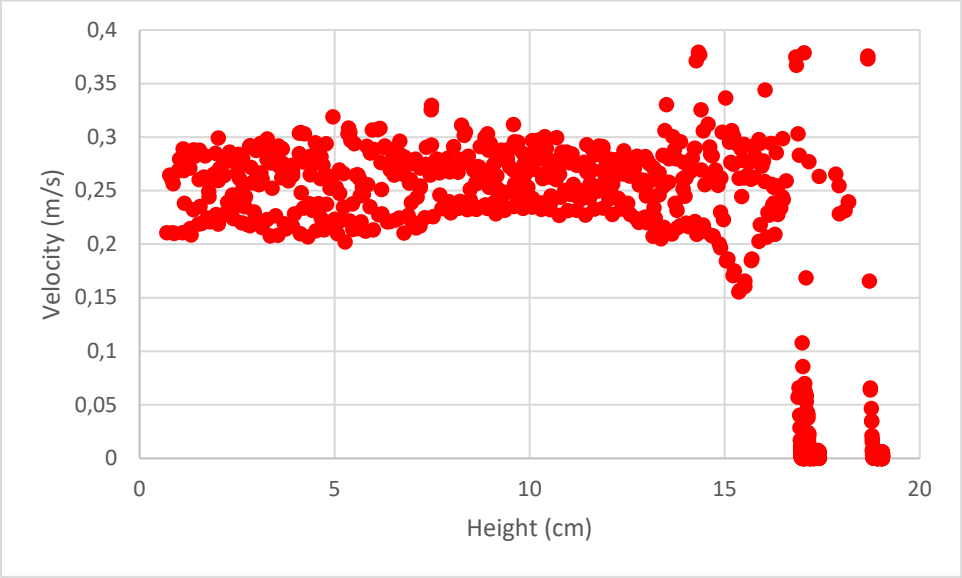

Figure 34 The velocity profile of bubbles rising in 0.15mol/L NaCl solution.

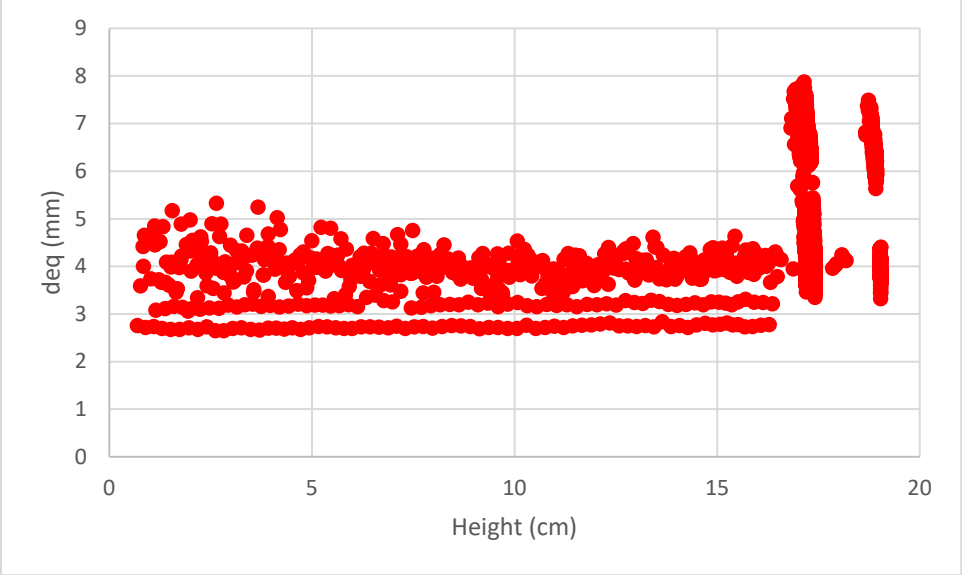

Figure 35 The equivalent diameter profile of bubbles rising in 0.15mol/L NaCl solution.

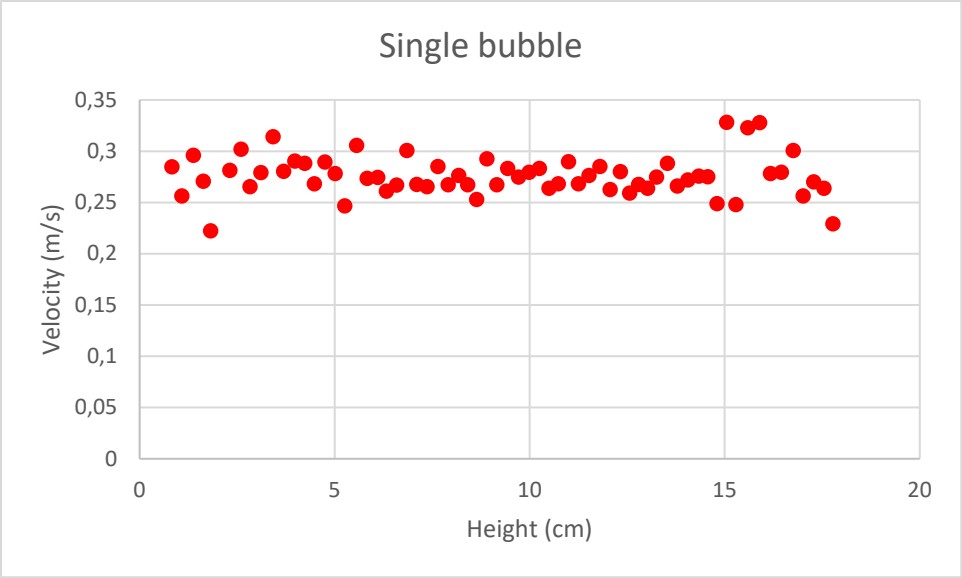

Figure 36 The velocity profile of a single bubble rising in 0.15mol/L NaCl solution.

B

Terminal velocity prediction by Fan and Tsuchiya

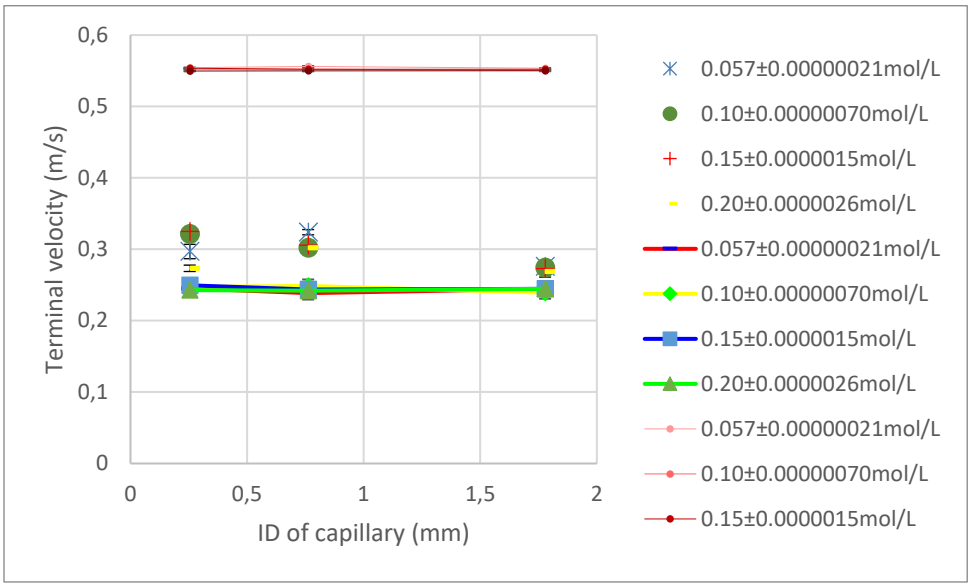

Figure 37 Terminal velocity predictions using Kb contaminated system.